LOCALIZATION PHENOMENA IN INAS/GASB COMPOSITE QUANTUM WELLS WITH DISORDER

by

VAHID SAZGARI ARDAKANI

Submitted to the Graduate School of Engineering and Natural Sciences
in partial fulfillment of
the requirements for the degree of
Doctor of Philosophy

Sabancı University
July 2019

LOCALIZATION PHENOMENA IN INAS/GASB COMPOSITE QUANTUM WELLS WITH DISORDER

APPROVED BY

Assoc. Prof. İsmet İ. Kaya
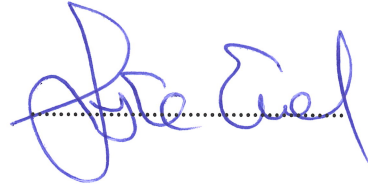(Thesis Supervisor)

....

Assoc. Prof. İnanç Adagideli

....

Assoc. Prof. Burç Mısırlıoğlu

....

Prof. Ayşe Erol

....

Prof. Ceyhun Bulutay

....

DATE OF APPROVAL   19/07/2019
....

ABSTRACT

LOCALIZATION PHENOMENA IN INAS/GASB COMPOSITE QUANTUM WELLS
WITH DISORDER

Vahid Sazgari Ardakani

Ph.D. Thesis, July 2019

Thesis Supervisor: Assoc. Prof. İsmet İ. Kaya

Keywords: Topological insulators, quantum spin Hall effect, quantum transport,
spintronics, localization

A bilayer structure of indium arsenide (InAs) and gallium antimonide (GaSb) has been
proposed as a two-dimensional (2D) electronic system tunable to different states of mat-
ter namely the trivial and the topological insulator (TI) phases. 2D TI which is also
called quantum spin Hall (QSH) insulator is characterized by an insulating bulk and
non-dissipative counterpropagating edge states with opposite spin polarizations. These
features identify the quantum spin Hall effect where the helical edge states are topo-
logically immune against backscattering guaranteed by time-reversal symmetry. Low-
temperature electronic transport measurements may serve to examine the transport prop-
erties of InAs/GaSb quantum wells and therefore to inquire into the essence of its bulk and
edge behavior. This work is aimed to study the constituents necessary to obtain a robust
quantum spin Hall insulator based on InAs/GaSb bilayer heterostructure. We focus on
the localization phenomena in InAs/GaSb bilayer quantum wells which are intentionally
disordered by silicon atoms. We observed that Si doping near the InAs/GaSb interface
significantly alters the transport behavior of these heterostructures.

First, we investigated the localization of trivial edge states driven by silicon impuri-
ties. As confirmed by recent experimental studies, conductance quantization due to non-
trivial edge states, which is the most significant highlight of the QSH effect is obscured
by spurious conductivity arising from trivial edge states. In this thesis, we present an ex-
perimental observation of the strong localization of trivial edge modes in an InAs/GaSb
heterostructure which is weakly disordered by silicon delta-like dopants within the InAs
layer. The edge conduction which is characterized by a temperature-independent behavior
at low temperatures and a power law at high temperatures is observed to be exponentially
scaled with the length of the edge. Results of comprehensive analyses on measurements

done with a range of devices are in agreement with the localization theories in quasi-one-dimensional electronic systems.

Spin-orbit interaction is one of the main ingredients of the TIs and in particular in disordered and thus low mobility electronic systems it leads to a weak anti-localization characteristic in low field magnetoconductance measurements. As the charge carriers are depleted using a top gate electrode, we observed a crossover from weak anti-localization (WAL) to weak localization (WL). This occurs when the dephasing length decreases below the spin-orbit characteristic length as a result of enhanced electron-electron interactions at lower carrier concentrations. The same crossover is observed with increasing temperature. The linear temperature behavior of inelastic scattering rate indicates that the dominant phase breaking mechanism in our 2D system is due to electron-electron interactions.

Finally, we compare three heterostructures (Wafers A, B, and C) all delta-doped with silicon atoms at different spatial positions in the growth direction near the InAs/GaSb interface. We found the transport behavior of these heterostructures to be very different from each other which can be attributed to the vertical position of disorder within the layered structures. Since the silicon atoms are donors to InAs and acceptors to GaSb, it matters where they are located with respect to the InAs/GaSb interface considering the interfacial effects and potential fluctuations induced by impurities.

ÖZET

DÜZENSİZLİK İÇEREN INAS/GASB KOMPOSİT KUANTUM KUYULARINDA YERELLEŞTİRME OLAYLARI

Vahid Sazgari Ardakani

Doktora Tezi, Temmuz 2019

Tez Danışmanı: Doç. Dr. İsmet İ. Kaya

Çift katmanlı InAs/GaSb kuantum-kuyu yapısı, normal yalıtkan ve topolojik yalıtkan fazları gibi maddenin farklı durumlarına ayarlanabilen 2-boyutlu bir elektron sistemi olarak önerilmiştir. İki boyutlu topolojik yalıtkanlar kuantum spin Hall yalıtkanı olarak da adlandırılır ve zıt spin polarizasyonlarına sahip yalıtkan bir kitle, ve birbirine zıt yönlü ve zıt spinli yitirgen olmayan iki kenar durumunun varlığı ile betimlenir. Kuantum spin Hall etkisini tarif eden bu helezon kenar durumları, zaman tersinmesi simetrisi sayesinde geri saçılmaya karşı topolojik olarak korunmalıdır. Düşük sıcaklıklarda gerçekleştirilen elektriksel ölçümlerle, InAs/GaSb kuantum kuyularının taşınım özellikleri incelemek ve dolayısıyla kitle/kenar davranışlarının özünü araştırmak mümkündür. Bu çalışmada InAs/GaSb çift katmanlı hetero-yapısında mukavemetli bir kuantum spin Hall yalıtkanı elde edebilmek için gereken farklı bileşenlerin incelenmesi amaçlanmıştır ve silikon katkılanarak düzensizleştirilmiş kuantum kuyularının taşınım davranışlarının değişimine ve yerelleştirme olaylarına odaklanılmıştır.

İlk olarak, silikon katkılanmasından kaynaklanan topolojik olmayan kenar durumlarının yerelleştirmesi etkisi araştırılmıştır. Son yıllardaki deneysel çalışmalarla da ortaya konulduğu gibi, kuantum spin Hall etkisinin en önemli özelliği olan topolojik kenar durumlarından kaynaklanan iletkenliğin nicemlenmesi olayı, sıradan kenar durumlarından kaynaklanan iletkenlik tarafından bozulmaktadır. Bu tezde, InAs katmanı içindeki silikon tek-katmanlı katkı atomları tarafından zayıf şekilde bozulmuş olan bir InAs/GaSb hetero-yapısı içindeki sıradan kenar durumlarının güçlü yerelleştirmeye gittiği deneysel olarak ortaya konmuştur. Düşük sıcaklıklarda, sıcaklıktan bağımsız bir davranış gösteren ve yüksek sıcaklıklarda bir kuvvet yasası ile orantılı olduğu belirlenen sıradan kenar iletkenliğinin, kenar uzunluğu ile ise üstel olarak ölçeklendiği belirlenmiştir. Çok sayıda ve

çeşitli aygıtlarla yapılan ölçümler kapsamlı analizinin sonuçları, 'sözde-bir boyutlu elektronik sistemlerde yerelleştirme' kuramları ile uyumludur.

Spin-yörünge etkileşimi, topolojik yalıtkanların en önemli özelliklerinden birisidir. Özellikle, düzensizliği nedeniyle düşük hareketliliğe sahip elektron sistemlerinde, spin-yörünge etkileşimi, düşük-alan manyeto-iletkenlik ölçümlerinde zayıf bir karşı-yerelleşmeye neden olur. Bu çalışmada yük taşıyıcıları bir üst-kapı elektrotu yardımıyla tüketildiğinde, zayıf-karşı-yerelleştirmeden zayıf-yerelleştirmeye bir geçişin ortaya çıktığı gözlemlenmiştir. Bu etki düşük taşıyıcı yoğunluklarında elektronlar arası etkileşimlerin artmasının bir sonucu olarak faz-kaybı uzunluğunun dönme yörüngesi karakteristik uzunluğunun altına indiği durumda ortaya çıkmakt adır. Bu geçiş, sıcaklığın artışı ile de ortaya çıkar. Esnek olmayan saçılma hızının doğrusal sıcaklık davranışı, 2-boyutlu elektron sistemindeki baskın faz kırılma mekanizmasının elektron-elektron etkileşimlerinden kaynaklandığını göstermektedir.

Son olarak, hepsi InAs/GaSb arayüzü yakınlarında olmak üzere, büyüme yönünde farklı konumlarda silikon atomlarının bulunan üç ayrı hetero-yapının elektriksel özellikleri karşılaştırılmıştır. Bu katmanlı yapılarda dikey düzensizlik konumuna atfedilebilecek birbirinden çok farklı taşıma davranışıları gözlemlenmiştir. Silikon atomları InAs içinde donör ve GaSb içinde alıcı olduklarından, arayüzey etkileri ve safsızlıkların neden olduğu potansiyel dalgalanmaları da dikkate alınca InAs/GaSb arayüzüne göre konumlarının çok önemli olduğu görülmüştür.

ACKNOWLEDGEMENTS

Contents

List of Figures and Tables

Chapter 1

INTRODUCTION

Topological Insulator (TI) is a new phase of matter that has attracted great interest not only for fundamental scientific research but also for its potential applications [1]. Particularly, the quantum spin Hall (QSH) insulator is a two-dimensional topologically nontrivial insulator. It is theoretically predicted to manifest an insulating bulk accompanied by dissipationless helical edge states. That is a pair of spin-polarized channels carries the charge around the sample's perimeter [2–5]. As a source of spinful quantum states, this new class of materials provide an ideal platform for novel spintronic applications, quantum information, and quantum engine [2–9]. The QSH effect was first predicted and soon observed in band inverted HgTe/(Hg,Cd)Te quantum wells (QWs) [3, 10, 11], where a transition from normal to topological phase can only be tuned by the thickness of the HgTe QW.

Over the past decade, InAs/GaSb heterostructures have been recalled by condensed matter physicists searching for a topological phase of matter namely the QSH insulator. Shortly after the realization of QSH effect in band inverted HgTe/(Hg,Cd)Te QWs, it was proposed that such a topological phase can also be hosted by InAs/GaSb bilayer quantum well structures with an inverted band configuration [12]. Bringing InAs and GaSb quantum wells together, the corresponding electron and hole carriers hybridize due to the inversion of InAs electron band and GaSb hole band. As a result of the coupling and hybridization of electron and hole wavefunctions, a small gap evolves in the crossing points of the two bands [12–14]. However, on account of the strong spin-orbit coupling (SOC), the bulk gap in such a system is accompanied by two counter-propagating topological edge states with opposite spin polarizations as characteristics of the QSH effect [2, 3, 12]. Enormous research efforts have been done to experimentally probe the electronic states in InAs/GaSb heterostructures with a focus on demonstration of spin-polarized helical edge conduction [15–35]. Among the new proposals for a QSH system, the InAs/GaSb bilayer QW heterostructure is favored as it benefits from high mobility, easy fabrication, and most importantly the tunability of the band structure by an electric

1

field [12, 15, 17, 19–23, 27, 28, 30]. Particularly, by application of dual gates on top and bottom of the heterostructure, the Fermi level and the alignment between InAs conduction and GaSb valence bands can be controlled independently in such a way that a continuous phase transition from trivial to broken-gap nontrivial insulator is possible [12, 23, 30].

Despite several reports on the observation of robust edge conduction, a clear-cut experimental confirmation of the quantum spin Hall effect in InAs/GaSb coupled quantum wells is still missing. The realization of the effect was soon found to be challenging by the presence of residual bulk conduction masking the possible helical edge modes [15, 17–23, 27, 28, 30]. The experimentalists came up with the idea of introducing some impurities inside the InAs/GaSb quantum channels and succeeded to some extent to localize the bulk carriers in the inverted regime [20–22, 36–39] also supported by some theoretical studies [40, 41]. Besides the non-zero bulk conductivity, a new obstacle has been recognized in recent experiments on these heterostructures. Diffusive edge modes have been proven to exist in the trivial regime of the InAs/GaSb bilayer quantum wells [27, 28, 42]. This implies that in future experiments, looking for quantum spin Hall effect, not only the helical nature of edge states needs to be confirmed but also the absence of trivial edge channels should be guaranteed, which may otherwise hinder the helical edge conduction.

In this doctoral thesis, we explore the effects of intentional silicon disorder on the edge and bulk transport properties of InAs/GaSb composite quantum wells among three wafers of similar structures with subtle difference in the position of impurity atoms in the growth direction. In particular, we focus on the elimination of trivial edge states via disorder-induced localization. Throughout this study, we realized that the relative distance of the silicon delta-like dopants from the InAs/GaSb interface is critically important. We have the Si atoms deposited during the InAs/GaSb epitaxial growth at a specific layer position with a density of 10^3 μm^{-2}. We have three heterostructures grown by molecular beam epitaxy (MBE) method, which are labeled as Wafers A, B, and C. Wafers A and B have Si doping inside InAs layer at respectively 2 atomic monolayer (ML) and 1 ML distance from the InAs/GaSb interface. Whereas in Wafer C, the Si atoms are deposited inside GaSb layer at 1 ML distance from the interface layer.

A background overview on quantum spin Hall effect and its experimental realizations is provided in chapter 2. The main outcomes of this thesis are presented in chapters 3, 4, and A. The thesis is concluded with a summary and outlook in chapter 5.

In chapter 3, we report on the localization of edge states in the trivial regime of InAs/GaSb bilayer QWs in Wafer A heterostructure. The bulk gap is tunable by gate electrodes on both sides of the quantum wells. Although the inverted regime where topological edge states are expected was not accessible in our heterstructure, the suppression

of trivial edge conduction is essential to achieve a robust quantum spin Hall effect in InAs/GaSb-based systems.

Chapter 4 contains our study on the spin-orbit interaction in disordered InAs/GaSb structures via WAL/WL phenomena observed in magnetotransport measurements of Wafer B.

Finally, all three heterostructures are compared with respect to their transport properties in Chapter A.

Chapter 2

OVERVIEW

For a long time, different phases of matter have been described by Landau theory which classifies them based on their different sorts of symmetry. According to this theory, a phase transition is driven by symmetry-breaking. However, condensed matter physicists introduced a new paradigm which proposes new quantum phases within the same symmetry group. These so-called topological states are characterized by another order parameter namely topological order which is not related to symmetry. For example, topological insulator (TI) is a class of topological materials with a non-trivial order parameter [1, 7]. TI's are especially intriguing because their bulk band structure supports peculiar surface states that are protected by time reversal symmetry. As a consequence, the surface states in a topological insulator, unlike the trivial insulator, conduct electrons freely without energy dissipation as long as the time reversal symmetry is preserved.

The integer quantum Hall effect (IQHE) [43, 44] is regarded as the first discovered topological phase of matter. A 2D conductor under strong perpendicular magnetic field transforms into a new state which is insulating in the bulk but conducting along the edges via non-dissipative helical edge modes. In this chapter, we discuss how IQHE inspired the physicists to build a 2D TI known as quantum spin Hall insulator [2, 4, 5]. A brief introduction to the quantum spin Hall effect (QSHE) and its experimental realizations are also given in this chapter. The main focus is dedicated to InAs/GaSb bilayer quantum wells which are the materials used in our study.

2.1. Quantum spin Hall effect

In the integer QHE, an external magnetic field applied normal to the plane of a 2D metallic system, discretize the energy band structure to Landau levels classically described as the cyclotron orbits. As a result, the electrons in the system occupy the Landau levels as the only allowed energy states. When the Fermi level lies in between two successive Landau levels, the bulk is insulating. However, the 1D chiral edge channels still conduct
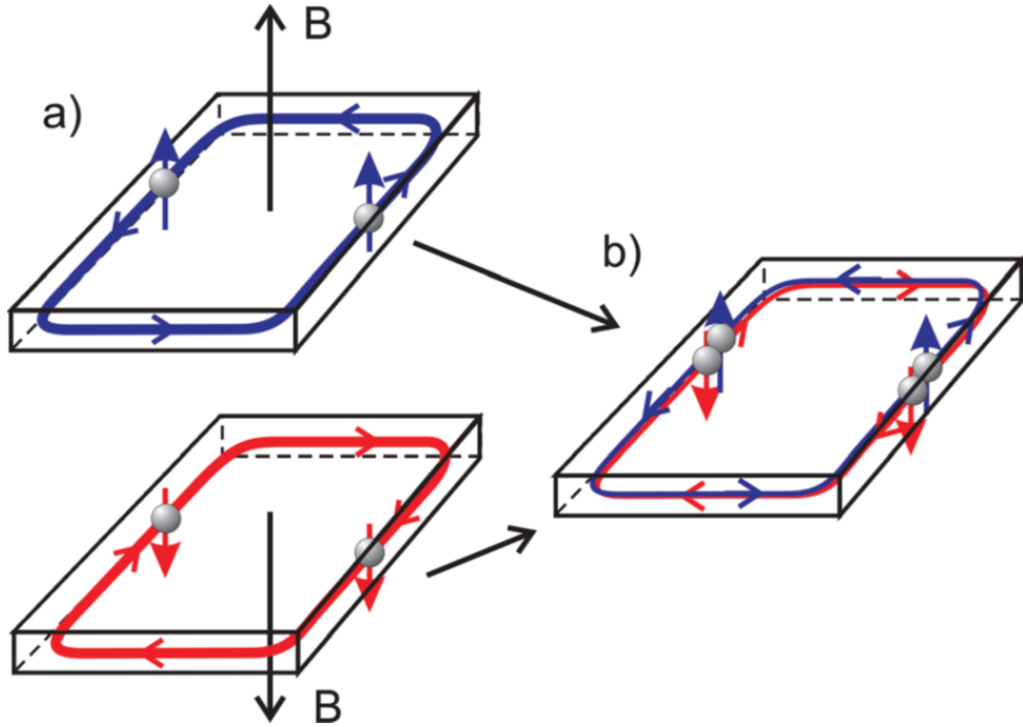
Figure 2.1: A combination of two $\nu = 1$ integer quantum Hall states with opposite magnetic field directions thus opposite chirality (a) is equivalent to a QSH state with helical edge channels at zero magnetic field (b). Adapted from Ref. [46].

the electrons without dissipation leading to precisely quantized Hall conductance ($\sigma_{xy} = \nu e^2/h$). The filling factor ν is defined as the number of occupied Landau levels and determines the number of chiral edge states. The QHE requires a magnetic field hence the time reversal symmetry is broken. In a thought experiment, two spin-polarized $\nu = 1$ quantum Hall systems with opposite magnetic fields can be combined to obtain a new quantum state at zero magnetic field which is therefore time reversal invariant. The result is a 2D topological system with an insulating bulk and a pair of counterpropagating helical edge modes with opposite spins. Such a topological phase at zero magnetic field is known as the quantum spin Hall insulator and was predicted by Kane and Mele in 2005 [45]. A schematic expression of integer QHE and QSHE is shown in Fig. 2.1.

The building blocks of a QSHI are band inversion and spin-orbit coupling (SOC) which preserves the time reversal symmetry. In a normal insulator, e.g. a conventional semiconductor, the conduction (electron) and valence (hole) bands are separated by a finite energy gap. Whereas in a QSHI, the electron and hole bands overlap. In this case the electron-hole coupling gives rise to a small hybridization gap forming a new band structure. Consequently, a hole-like band lies above an electron-like band spaced by a minigap.

According to topological band theory, gapless edge states must exist at the interface between different topological phases. Fig. 2.2 displays schematic band structure in trivial
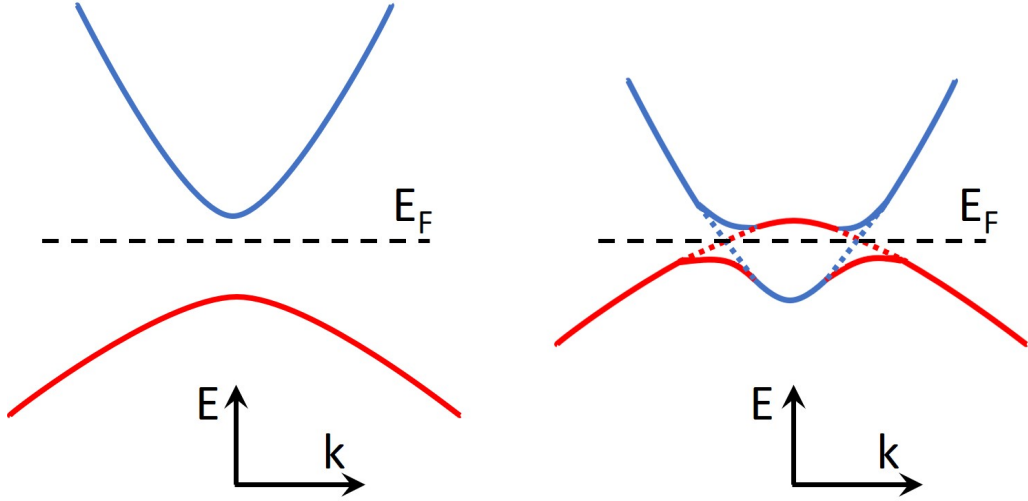
Figure 2.2: Band line-up for trivial (left) and non-trivial (right) insulators with normal and inverted bulk gaps, respectively. Conduction (electron) band is shown in blue and valence (hole) band is depicted in red color.
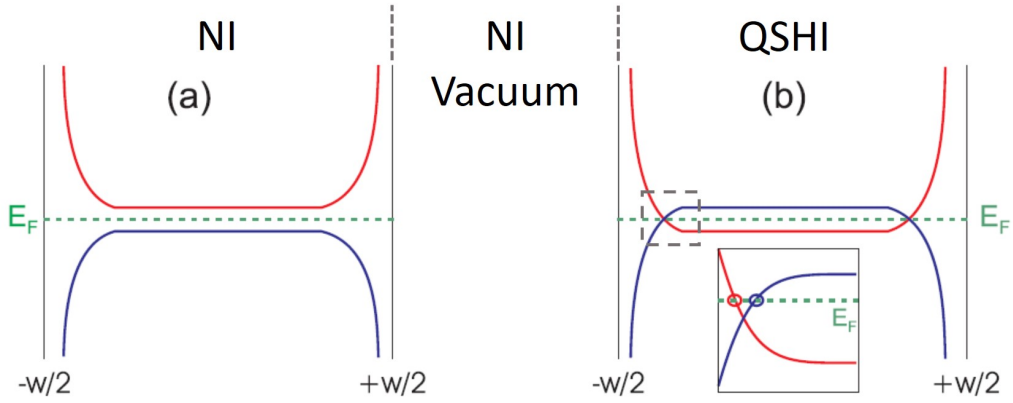
Figure 2.3: (a) Trivial band insulator without edge states at the vacuum interface. (b) non-trivial edge states are formed at the boundary of a QSHI and a normal insulator (vacuum). Inspired from [47].

and inverted band alignments. In both cases, when the Fermi energy is inside the gap, the bulk is insulating. However, at the boundary between a QSHI and a normal insulator (e.g. vacuum), the inverted bands in continuity to normal band alignment have to cross each other forming gapless edge states with linear dispersion. This simple explanation of the edge state formation at the interface of topologically different insulators is pictured in Fig. 2.3. The linear energy dispersion of these edge states is governed by the mass continuity. The mass inside the QSHI is positive (negative) for inverted hole (electron) bands, whereas in vacuum (or any normal insulator) the mass is negative (positive) for hole (electron) bands. In fact, the mass changes the sign in crossing the interface between an inverted and a normal band structure. Thus at the edge (interface), the mass has to be zero as for a Dirac fermion.

The topological edge states which are protected by time reversal symmetry, are ab-

sent in a normal insulator. However, trivial edge modes are still allowed in both phases. Indeed, one can distinguish a QSH phase from a normal insulator phase directly by looking at the edge state spectrum. An odd (even) number of Kramers pairs of edge states indicates a QSH (normal) insulator [12]. Kramers theorem necessitates that every energy state of a system with half-integer spin is at least two-fold degenerate if the time reversal symmetry is preserved ($\vec{k} \longleftrightarrow -\vec{k}$). Therefore, at Γ point ($\vec{k} = 0$), there has to exist at least one Kramers pair. In fact, the two edge states intersect at $\vec{k} = 0$.

Recalling the QH state, the Kramers double degeneracy is lifted because the time-reversal symmetry is broken by magnetic field. Therefore at the interface of a QH insulator (i.e. a topological phase) and a normal insulator, only one edge state will be remained (Fig. 2.4). But in a QSHI which is time-reversal-symmetric, a pair of edge states is guaranteed by Kramers degeneracy theorem [1]. A schematic representation of the chiral edge state in QH and helical edge states in QSH is illustrated in Fig. 2.4. It should be noted that the edge states in QSHI are helical that is spin-polarized and counterpropagating. This is a concomitant of spin-orbit coupling in combination with time-reversal symmetry. The SOC lifts the spin degeneracy which indicates the spin-polarization, and time-reversal operation flips both spin and momentum directions implying counterpropagation of edge states.

Spin-orbit coupling is time-reversal invariant and locks the spin of electron to its momentum. As sketched in Fig. 2.3, the electron in a QSH edge state can be backscattered in two opposite time-reversed directions along an intersecting path. In one direction the spin rotates by π and in the other direction rotates by $-\pi$. In the net spin rotation of 2π, the electron's wavefunction acquires a phase factor of -1 leading to a destructive interference. Therefore, the helical edge states in a QSHI, are protected against backscattering by time-reversal symmetry. In other words, the helical edge states are dissipationless and carry one quantum conductance (e^2/h) each.

2.2. Experimental realizations

The QSH effect was first proposed for graphene by Kane and Mele in 2005 [2]. However, it could not be observed experimentally due to weak SOC and therefore small hybridization gap (on the order of μV) [48, 49]. Since then, new candidates with sufficiently strong SOC have been proposed [3, 12]. In spite of several proposals for realization of the QSH phase, so far only three material systems are rigorously studied experimentally with the aim to observe a robust QSH phase: HgTe/(Hg,Cd)Te quantum well, InAs/GaSb composite quantum wells, and monolayer WTe_2 [50].
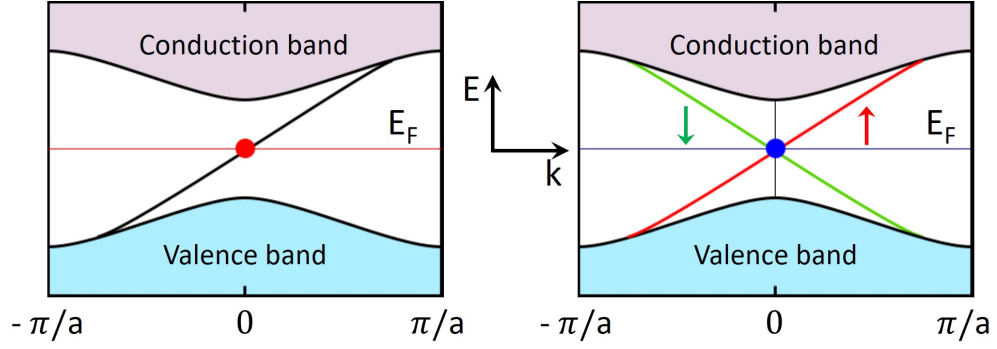
Figure 2.4: QH vs QSH insulators. Left: integer quantum hall is characterized by an insulating bulk with a single right-mover or left-mover edge state depending on the B field direction. Right: A QSHI with a bulk gap and two counterpropagating edge states which has to be spin-polarized due to time-reversal symmetry. Adapted from [1]

2.2.1.   HgTe-based quantum wells

The first experimental realization of QSHE was reported in HgTe/(Hg,Cd)Te quantum well [10]. It was theoretically predicted a year earlier by Bernevig, Hughes, and Zhang that a HgTe quantum well wider than a critical value would be band-inverted and therefore a QSHI [3]. The topological phase of this QW is determined by an intrinsic parameter i.e. the QW thickness thus any individual device would have either a normal or a topological band order. The robust edge conduction was confirmed in these QWs via local and non-local measurements with expected quantized conductances in different configurations for short edges. Also, through the combination of QSHE and inverse spin Hall effect, the spin-polarization of edge states in QSH regime has been studied [46].

2.2.2.   InAs/GaSb composite quantum wells

The motivation for a semiconductor material extrinsically tunable to different topological phases led to the introduction of a new candidate: InAs/GaSb double quantum well. In 2008, Liu et al. [12] proposed that the combination of an electron gas in InAs and a hole gas in GaSb, confined by AlSb barrier, would demonstrate an electronic system with a rich phase diagram including a QSH regime.

These heterostructures contain semiconductor materials which belongs to the so-called 6.1 Å family [51]. They have quite the same lattice constant and therefore similar crystal structures. InAs/GaSb/AlSb form approximately a lattice matched heterostructure facilitating an epitaxial growth. Despite the similar crystal structure, they have very different band parameters and energy gaps from 0.36 eV for InAs to 1.61 for AlSb. Bringing the bulk materials together, their bands line up in the way shown in Fig. 2.5. The AlSb with a large energy gap is an ideal barrier material to confine InAs, GaSb, and InSb quantum
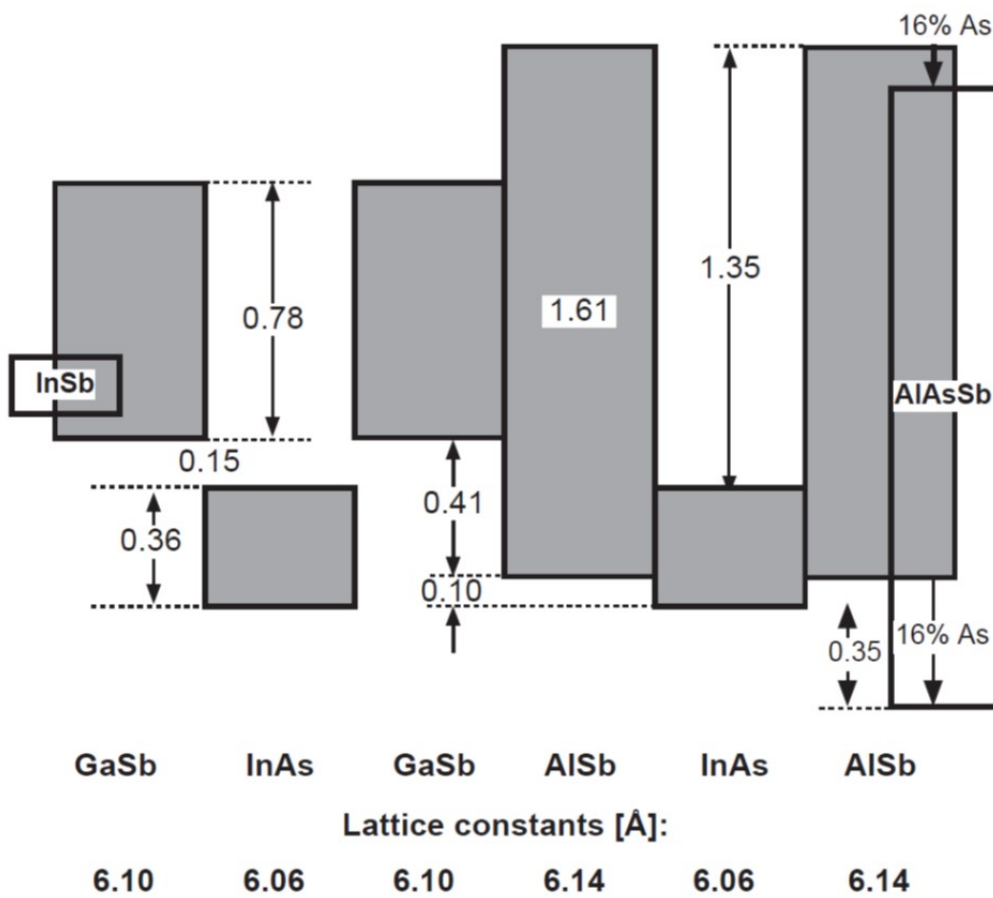
Figure 2.5: Band lineups for 6.1 Å family. The gray areas represent the energy gap and all energies are in eV unit. Adapted from Ref. [51].

wells. Notably, the conduction (electron) band of InAs lies below the valence (hole) band of GaSb for bulk materials. Therefore, InAs/GaSb/AlSb can form a combined semiconductor structure with inverted band alignment.

However, the exact offset between electron and hole bands in bilayer InAs/GaSb is determined by the relative thickness of the electron/hole quantum wells and also by an electric field in the growth direction [12]. Although, the electrons and holes in InAs/GaSb composition live in spatially separated quantum wells, they can interact when their corresponding wavefunctions overlap. Naveh and Laikhtman [52] demonstrated the coupling between the electron and hole gases in separate InAs and GaSb layers when their bands are inverted. They hypothesized that the bands hybridize and form a small gap at their crossing points in momentum space as a result of coupling through interlayer charge transfer. They also showed a vertical electric field can push the electron and hole bands in opposite directions so that by changing the electric field one can tune the band alignment from inverted to non-inverted and vice versa as demonstrated in Fig. 2.6.

Assuming the inverted configuration, the coupling strength and therefore the hybridization gap depend on the thicknesses of the InAs/GaSb quantum wells. For rather wide (thick) quantum wells, the electron and hole bands are localized in the center of their respective QWs far from the InAs/GaSb interface which means a weak coupling. Reducing the layer thicknesses, the wavefunctions start to overlap therefore a hybridization of bands may occur at their crossing point $\vec{k}_{cross}$. The expected hybridization gap is of the order of few meV which is much smaller than the band overlap.

To probe the exotic properties of this combined electronic system in transport experiments, one should be able to tune the Fermi level and band alignment independently. A dual gate configuration was predicted to provide such a tuner tool [12] schematically shown in Fig. 2.7.

Also verified experimentally, the electrostatic gates on both sides of the composite InAs/GaSb QW, implemented on top and bottom of the heterostructure, provide the desired electric field and potential within the QWs [23, 30, 35]. A theoretical and an experimental demonstration of the phase diagram mapped by a dual gate configuration are illustrated in Fig. 2.8. A plenty of electronic regimes from electron or hole-type metallic to normal and QSH insulator regimes is accessible within a range of applied gate voltages on top and bottom. The electric field which tunes the band lineup is proportional to the difference of the two gate voltages within some coefficients $(V_f - V_b)$. On the other hand, the Fermi level is independently adjustable by the sum of the gate voltages $(V_f + V_b)$. The tunable phase diagram utilizing external parameters is the main advantage of the InAs/GaSb-based QSHI over the other proposed systems. The ability to switch on
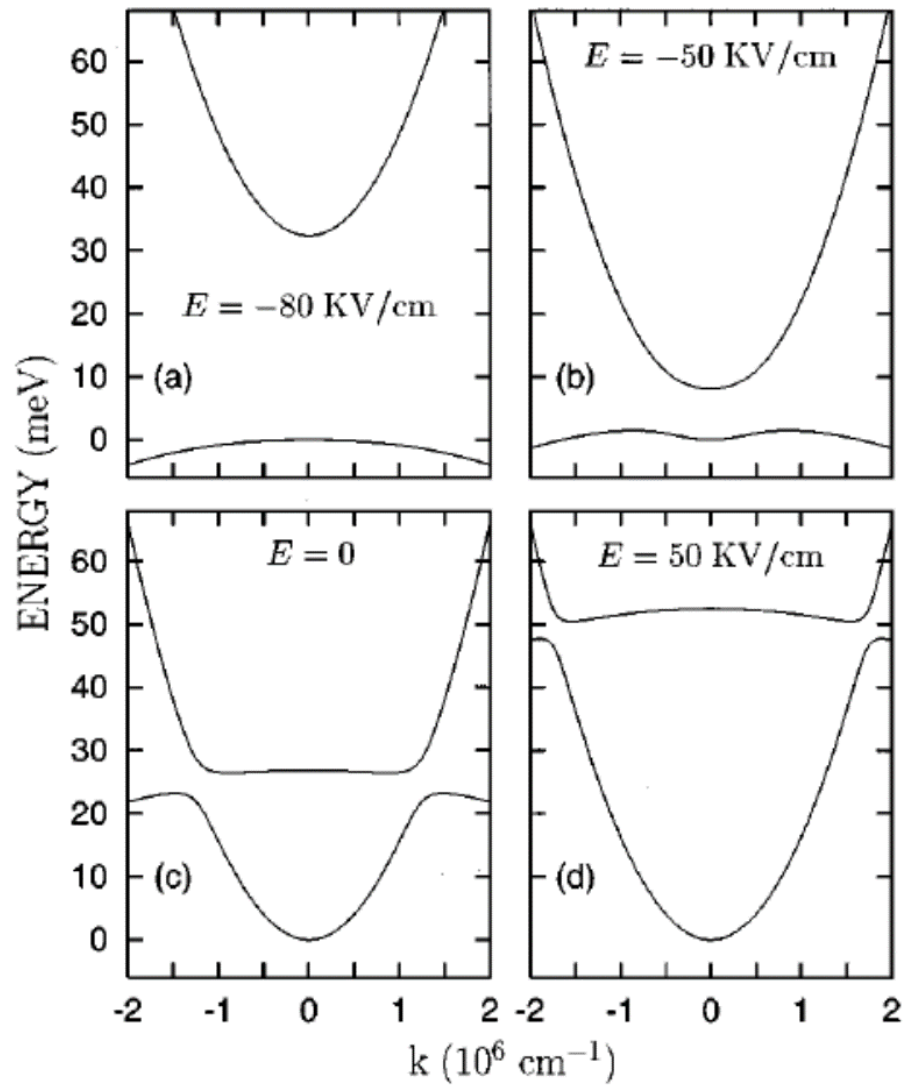
Figure 2.6: Band engineering of InAs/GaSb bilayer QWs using an external electric field. Adapted from Ref. [52].
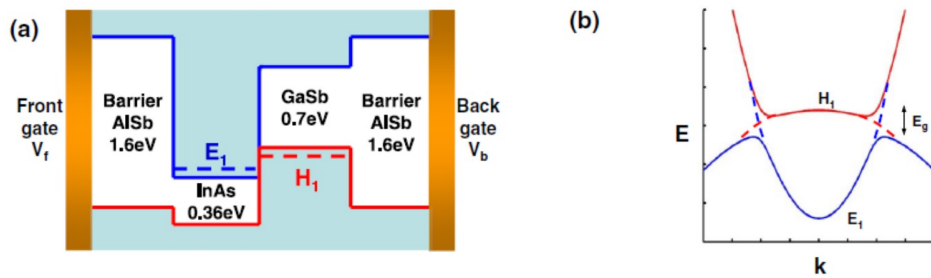
Figure 2.7: (a) A schematic of a dual gate configuration connected to top and bottom AlSb barriers. (b) Band structure diagram in the inverted regime with electron and hole subbands crossing and hybridize at a non-zero momentum. Adapted from Ref. [12].
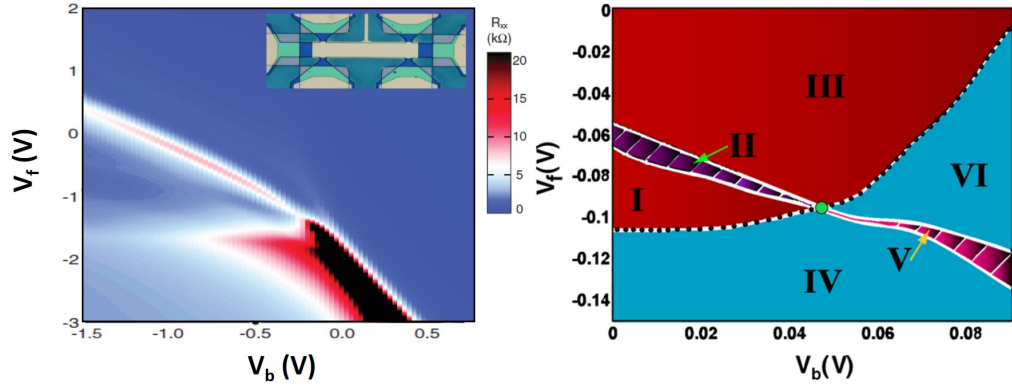
Figure 2.8: Right: The phase diagram as a function of top and bottom gate voltages calculated numerically. Adapted from Ref. [12]. Left: The phase diagram obtained in a transport experiment. Adapted from [23]

or off the QSH edge conduction in a dual-gate geometry, motivated the realization of a QSH field effect transistor.

2.2.3. WTe$_2$

Recently, a QSH phase with a large gap of about 100 K is reported in monolayer tungsten ditelluride WTe$_2$ [50]. However, the quantized conductance was observed in short-edge limit for edge lengths below $\sim$ 100 nm.

The enthusiasm towards the realization of a room temperature QSHI motivates an extensive theoretical and experimental research for new material systems.

Chapter 3

LOCALIZATION OF TRIVIAL STATES ALONG DISORDERED EDGES

In this chapter, we investigate the transport behavior of the trivial edge states in bilayer InAs/GaSb QW structures. As confirmed by recent experimental studies, the most significant highlight of the QSH effect i.e., the conductance quantization due to non-trivial edge states is obscured by spurious conductivity arising from trivial edge states. After providing a historical background on edge transport studies in InAs/GaSb heterostructures, we present experimental observation of strong localization of trivial edge modes in an InAs/GaSb heterostructure which was weakly disordered by silicon delta-like dopants within the InAs layer. While the 2D bulk transport properties are not affected by the silicon impurity, the edge states are strongly influenced by disorder. The edge conduction which is characterized by a temperature-independent behavior at low temperatures and a power law at high temperatures is observed to be exponentially scaled with the length of the edge. Comprehensive analyses on measurements with a range of devices is in agreement with the localization theories in quasi one-dimensional electronic systems [35].

3.1. Previous edge transport studies

The QSH effect was first predicted and soon observed in band inverted HgTe/(Hg,Cd)Te quantum wells (QWs) [3, 10, 11], where a transition from normal to topological phase can only be tuned by the thickness of the HgTe QW. Among the new proposals for a QSH system, the InAs/GaSb bilayer QW heterostructure is favored as it benefits from high mobility, easy fabrication, and most importantly the tunability of the band structure by an electric field [12, 15, 17, 19–23, 27, 28, 30]. Particularly, by application of dual gates on top and bottom of the heterostructure, the Fermi level and the alignment between InAs conduction and GaSb valence bands can be controlled independently in such a way that a continuous transition from trivial to broken-gap nontrivial insulator is possible [12, 23].

In the early experiments on InAs/GaSb double QWs, the edge conduction was over-
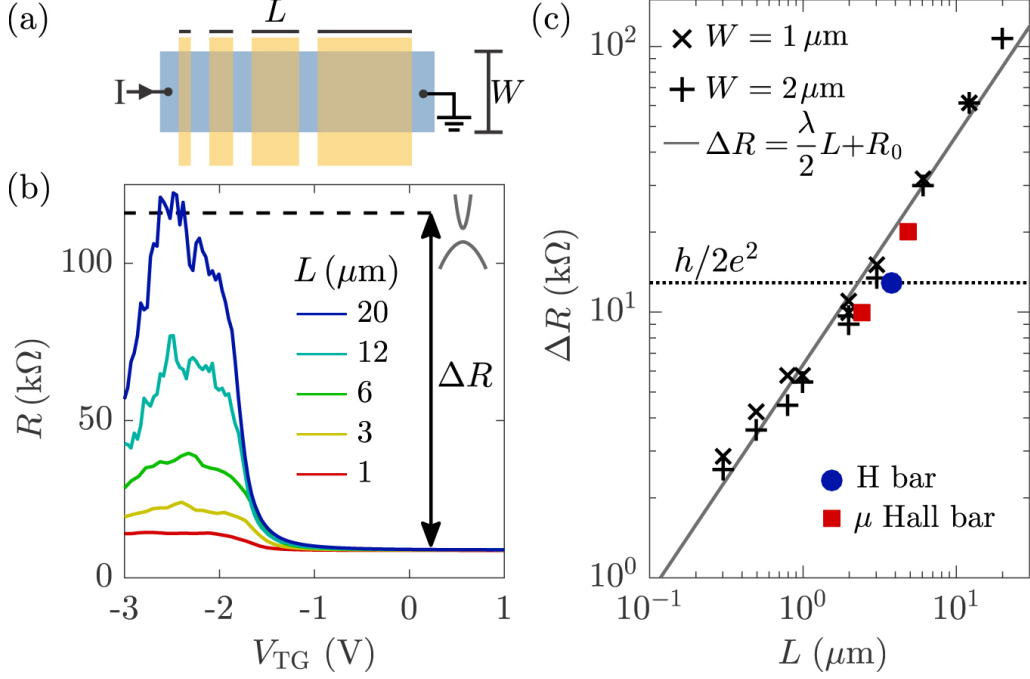
Figure 3.1: The edge resistance of an InAs/GaSb heterostructure in the trivial regime. (a) Schematic representation of finger gate device used to measure the length-dependent resistance of the edge channels. (b) Resistance of a finger gate device with a width of 2μ m as a function of top gate voltage for gated regions of different lengths. (c) Resistance change vs gate length shows a linear behavior without saturation at short edge limits. Adapted from Ref. [27].

shadowed by relatively large residual bulk conductance [15]. Subsequent efforts to suppress the bulk conductance via localization of bulk carriers incorporated the introduction of Si impurities at the interface between InAs and GaSb quantum wells [20–22], Be doping in the QW barrier [36, 37], or using low purity Ga source material for the GaSb layer [38, 39]. These studies confirmed robust edge transport, however whether the conduction was due to helical or trivial edge states was not proven. On the other hand, more recent works demonstrated the presence of edge transport also in the trivial phase of these heterostructures [27, 28, 42]. The possible coexistence of non-helical and helical edge channels in InAs/GaSb bilayers in the inverted regime may obscure the QSH effect and thus demands further experimental efforts for the elimination of trivial edge conductance.

3.2. Trivial and topological edge states

The trivial edge states can be distinguished from topological edge modes by comparing their band structures. A schematic of trivial and topological band structure is represented in Fig. 3.2. The topologically protected edge states are characterized by an odd number of Kramers pairs whereas an even number of Kramers pairs (including zero) indicates a trivial band structure [12, 53]. It can be shown that for an odd number of Kramers pairs,
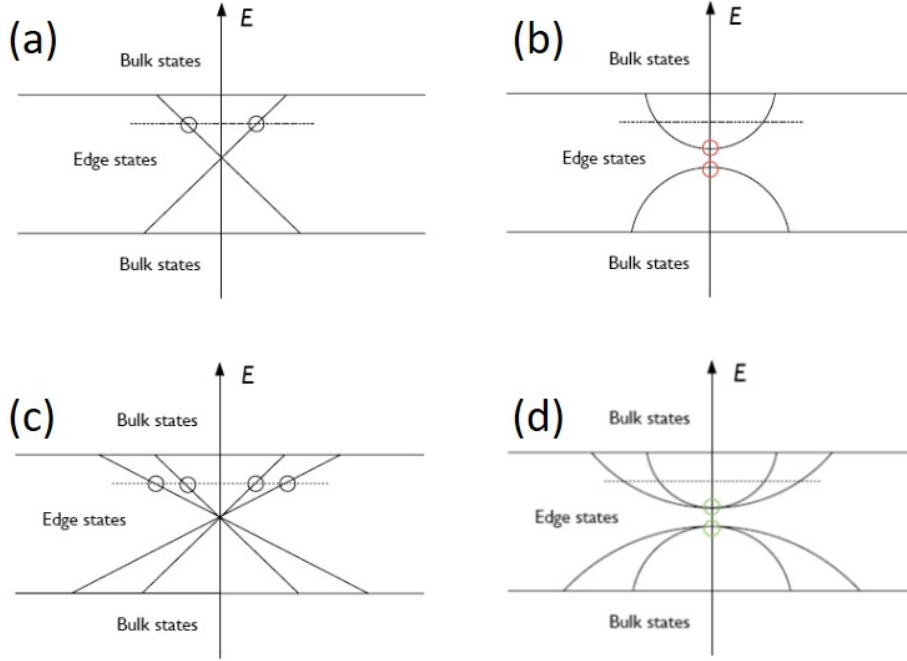
Figure 3.2: Schematic of topological and trivial edge states. (a) A single pair of Kramers pair forms the topological edge states crossing each other at $\vec{k} = 0$. (b) Gapped trivial edge states when there is no Kramers pair inside the bulk gap. (c) Gap-less trivial channels as a result of even pair number of Kramers states. (d) Similar to (c) but with a gap in trivial edge states.

there is always at least one pair of edge modes which are topologically immune against disorder. That is the transmission probability of these non-trivial edge states through a disordered region of the sample's edge is unity as long as the the time reversal symmetry is not broken. Unlike the topological edge states, the normal (trivial) edge states are not protected against disorder. In this case, the backscattering is possible leading to a dissipative transport along the edges. This property allows the localization of trivial edge modes by an arbitrary disorder. The realization of a pure QSH insulator would require no trivial edge transport if possible, or its suppression via e.g. the localization by disorder at the edge.

Several experiments with different sample geometries and edge lengths have shown that the edge transport is nearly identical in trivial and inverted phases of the InAs/GaSb heterostructures, where the edge resistance consistently increased with the edge length in a linear fashion [27, 28, 42]. A robust edge conduction has been observed also in InAs single QWs [42, 54]. Indeed in all of these measurements, the edge resistance per unit length was λ = 2-10 kΩ/μm in both trivial and inverted regimes. Measured resistance plateaus situated well below h/e^2 for small samples evidenced for multi-mode non-helical edge states. The magnitude of the trivial edge resistance is found to be sample dependent. It is believed that the trivial edge conduction is originated from band structure effects, such as band bending at the vacuum interface, fabrication-induced spurious effects, or

concentrated electric field at the edges of the sample induced by the top gate covering the side walls of the device mesa [27, 28, 42]. Moreover, the nature of trivial edge conductance has been identified to be *n* type as it is observed in both single InAs and double InAs/GaSb QWs [27, 28, 42, 54].

The conduction band of InAs bends down at its surface or interface with other materials with the Fermi level pinned above the conduction band edge [55–57]. This band bending which can be of the order of InAs bulk gap would results in accumulation of electrons at the surface or interface. The similar edge conduction observed in InAs and InAs/GaSb suggests that it is likely originated from InAs band bending at its interface with the dielectric layer used for passivation of the etched edges. Suppression of the resulting trivial edge conduction would require a reduction of band bending to values sufficiently smaller than the bulk energy gap either in trivial or topological regimes. Sample processing and passivation techniques strongly influence the amount of band bending and therefore the trivial edge resistance [28, 54]. For example, using the atomic-layer-deposited Al_2O_3 is found to be most effective in suppression of trivial edge conductance compared to other passivation methods such as SiN or sulphur passivation [54].

The spurious effects due to fabrication processes may also lead to the edge conduction. The residual amorphous Sb redeposited after the etching of AlSb-based barriers or the dangling bonds can form conducting channels at the edges of the mesa leading to a trivial edge conduction. Optimized etching recipes and various passivation techniques were proposed to reduce these fabrication-induced effects [58–60].

An alternative scenario explains the edge transport via the different effective electric field on the bulk and at the edges of a device. In standard fabrication recipes, the top gate is deposited after the mesa etching and passivation. Therefore, the top gate electrode covering the mesa surface and walls would induce different capacitance on the surface and at the etched walls, which results in an enhanced electric field at the edges [61]. Consequently, at a corresponding top gate voltage when the bulk is insulating, the edge can become conducting [27].

In conclusion, the existence of trivial edge conduction is likely in the InAs-based quantum well structures either due to band structure or fabrication-induced effects. The trivial nature of these edge states allows one to deplete or eliminate them. Using a side gate to deplete the edge states is shown to be effective in reducing the edge conduction to some extent though it can not eliminate it [62]. Alternatively, the trivial edge modes can be localized by an arbitrary disorder because they are not protected against impurity [35]. We have shown that Si impurities deposited inside the InAs layer in Wafer A could significantly suppress the edge conduction via localization of the edge carriers.
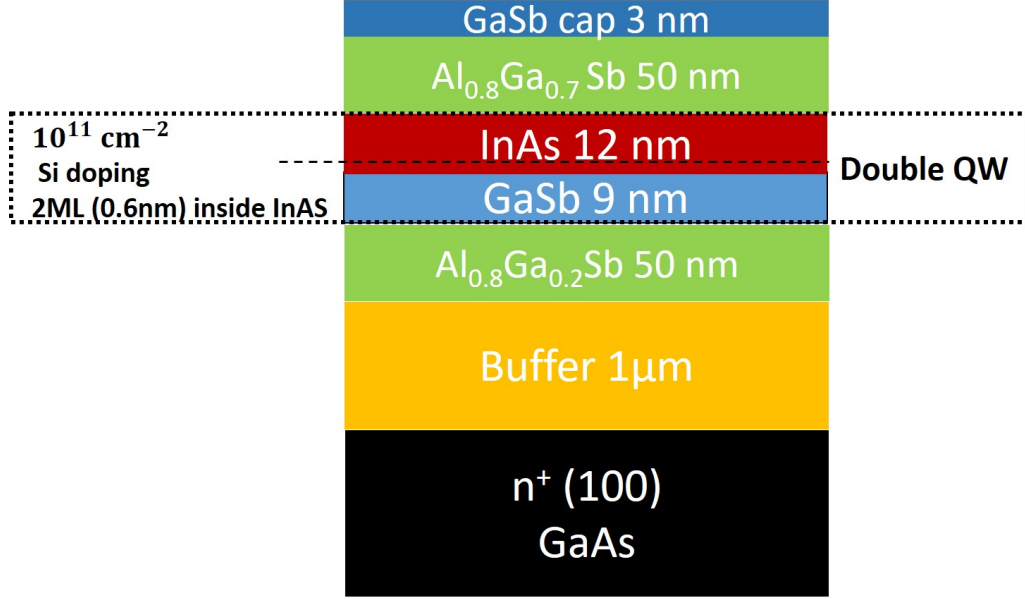
Figure 3.3: Wafer A: Schematic of the heterostructure measured and presented in this chapter with Si delta-dopants inside InAs QW at 2 monolayer distance from the InAs/GaSb interface.

3.3. Wafer structure, device fabrication, and measurement setup

The wafer material of this study, which we call Wafer A, was grown on a GaAs substrate by molecular beam epitaxy as it is depicted in Fig. 3.3. Following a 1-μm-thick AlGaSb buffer layer, the bilayer QW structure was grown, which consists of 12 nm InAs on 9 nm GaSb sandwiched between top and bottom AlGaSb barriers of 50 nm. Silicon atoms, as a single layer impurity, were added in the form of delta doping during the growth of InAs layers. The Si particles with an average density of 1×10^{11} cm^{-2} were deposited inside the InAs at 2 atomic monolayer distance from the InAs/GaSb interface. The top barrier was protected from oxidization by a 3 nm GaSb cap layer. A 20×5 μm ($L \times W$) Hall bar device with uniform gate, a 150×10 μm Hall bar with finger gates and a Corbino disk which is top-gated by a ring-shaped metal with inner and outer diameters of $r_i = 400$ μm and $r_o = 600$ μm respectively were used in the measurements. The device mesas were patterned by standard electron beam lithography and defined via chemical wet etching. The etched surfaces were passivated by a 100 nm plasma-enhanced chemical vapor deposition (PECVD)-grown Si$_3$N$_4$ layer which also served as the dielectric separating the Ti/Au top gate electrodes from the heterostructure. The ohmics were made by Ge/Au/Ni metalization without annealing. Transport measurements were performed in a dilution refrigerator with a base temperature of 10 mK using standard lock-in methods with 10 nA current excitation at 11 Hz, unless otherwise stated.

3.4.   Transport studies

3.4.1.   Hall bar device: Local and non-local resistance measurements

The phase diagram of the InAs/GaSb composite quantum well was obtained by measurements of the longitudinal resistance while sweeping the top and bottom gate voltages within the ranges at which the leakage through the bottom gate was less than 1 nA. Fig. 3.4(a) represents the longitudinal resistance of the Hall bar sample as a function of top gate, V_{tg} and bottom gate, V_{bg} voltages. Within the extent of the applicable gate voltages, the sample remains in the normal phase where the trivial gap decreases with decreasing V_{bg}. The tunability of the system was restricted within the trivial regime due to current leakage through the bottom gate for $V_{bg} < -1.8$ V. The longitudinal resistance in the electron-rich region is about 1 kΩ and sharply increases by four orders of magnitude and the system becomes insulating when the Fermi level is tuned inside the normal gap. Thereafter, the resistance decreases as the top gate voltage is decreased and the system is moved into the hole regime, nevertheless remaining significantly higher than that of the electron side due to lower mobility and charge density. The Hall resistance measurements performed at $B = 0.5$ T were used to extract the carrier density at different gate voltages. The modulation of longitudinal resistance and the carrier density by the top gate is shown in Fig. 3.4(b) for $V_{bg} = -1.8$ V. As V_{tg} is swept towards negative voltages, the electron density continuously decreases to zero until the Fermi level lies inside the bulk gap where the longitudinal resistance peaks around 4 MΩ. By further decreasing V_{tg}, the hole carriers are populated, though with low concentration, but below $V_{tg} = -9$ V, the carrier density slightly decreases. We attribute this to the electron release and capture in the trap states induced at the interface of GaSb and insulator layer, or the hole states induced in the GaSb cap layer, which screen the electric field from the top gate voltage [63, 64].

Furthermore, we performed quantum Hall measurements in the Hall bar device. As it is shown in Fig. 3.5, in the electron regime, Shubnikov-de Haas (SdH) oscillations in the longitudinal resistance and well-established quantum Hall plateaus indicate a high mobility 2D electron gas in the InAs QW. The electron mobility of the sample is calculated as $\mu = 1.5 \times 10^4$ cm^2/Vs at the density of $n = 1.0 \times 10^{12}$ cm^{-2}. Assuming this mobility, the elastic mean free path is obtained as $l_e = 30\ nm$ which is consistent with the mean spacing between single Si scatterers recalling that the 2D density of the silicon impurity is 10^{11} cm^{-2}. Therefore, we conclude that the silicon atoms are the dominant scattering centers leading to localization of the carriers hence an insulating behavior.

The Hall bar device exhibits a robust non-local signal as displayed in Fig. 3.6(a), which manifests conduction by edge states. As discussed below, comparison of the local
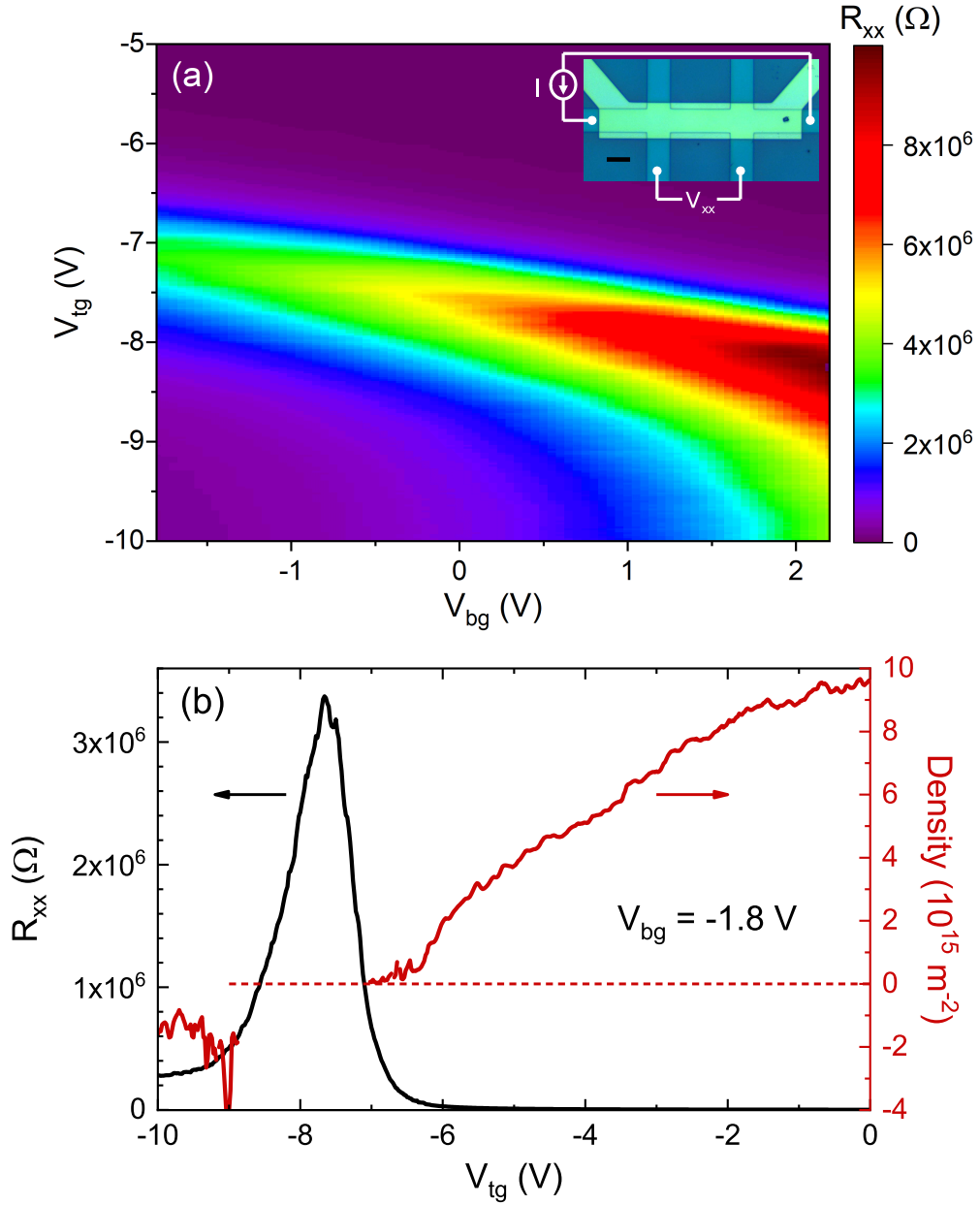
Figure 3.4: (a) Longitudinal resistance of the Hall bar device as a function of V_{tg} and V_{bg} measured at $T = 10$ mK applying 10 nA DC current. Inset shows the optical microscope image of the device with a 5-μm black scale bar. (b) Density modulation via top gate obtained from Hall measurements at 0.5 T (red curve). The dashed guideline indicates the zero density. The black curve shows the corresponding longitudinal resistance at B=0.
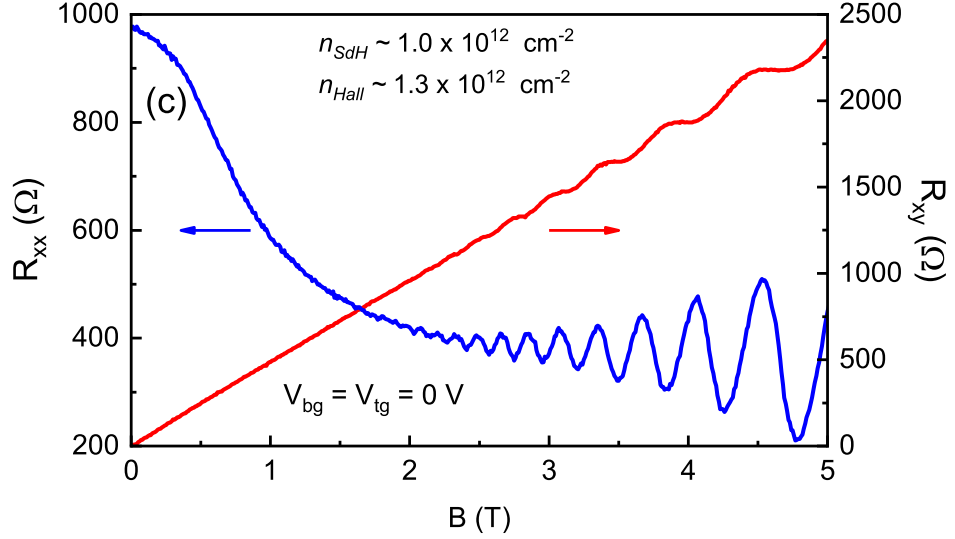
Figure 3.5: Longitudinal and transverse resistances as a function of B measured at 10 mK. As a signature of high mobility, clear SdH oscillations and quantum Hall plateaus are observed. The carrier densities calculated from quantum Hall and SdH oscillations are consistent with the one obtained from classical Hall effect in Fig. 3.4(b).

and non-local signals together with the results from the Corbino device confirm that the conduction in the Hall bar within the gap is predominantly governed by the edge states. Fig. 3.6(b) compares the local and non-local resistances, with bottom gate at 0 V, as the top gate voltage is swept from electron-rich regime to the normal gap and further to the hole band. Deep in the electron regime, the non-local resistance becomes less than the measurement sensitivity and practically orders of magnitude smaller than the local resistance. The ratio between local and non-local resistances is more than 3 orders of magnitude in the measurable range in the electron side. Inside the gap, on the other hand, since the bulk conductance is suppressed while the edge is conducting, the non-local signal is magnified to within an order of magnitude of the local signal.

3.4.2. Bulk gap measurement using Corbino geometry

In order to quantify the suppression of bulk conductance in the Hall bar device, we investigated a Corbino geometry in which the current flows radially between inner and outer contacts entirely in the bulk. The bulk conductivity of the Corbino disk is measured as a function of top and bottom gate voltages at different temperatures.

The phase diagram of the bulk state is obtained by measuring the resistivity of the Corbino device at varying top and bottom gate voltages. At very low temperatures the maximum resistance in the gap regime was immeasurably large. Only at sufficiently high temperatures we could measure the bulk resistance when the Fermi level lies inside the gap. The gate-controlled phase diagram is illustrated in Fig. 3.7(a). The minimum
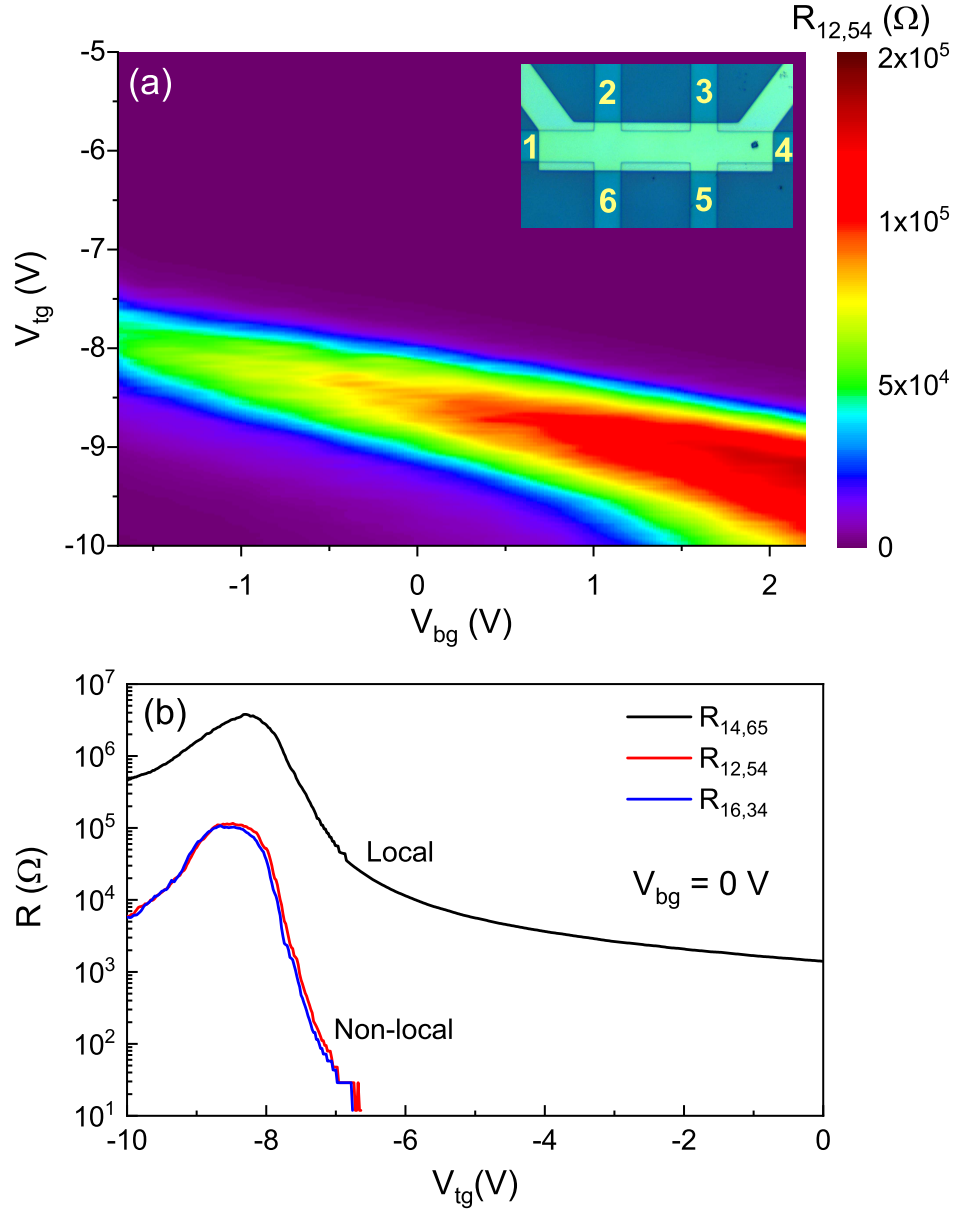
Figure 3.6: (a) Non-local resistance measured in the Hall-bar device as a function of top and bottom gate voltages at 10 mK. Inset shows the optical image of the device with labeled contacts. $R_{ij,kl}$ is the resistance measured between k and l when the current applied between i and j. (b) Comparison of local and two different configuration of non-local resistances as functions of top gate voltage.

conductivity in top gate sweep, which we referred to as the bulk conductivity, is calculated by $\sigma_{bulk} = (I/2\pi V)\ln(r_i/r_o)$ for the ring geometry. σ_{bulk} scales exponentially with the inverse of temperature as can be seen in Fig. 3.7(b). We calculated the bulk gap, Δ from the Arrhenius law, $\sigma_{bulk} \propto \exp(-\Delta/2k_B T)$ where the fitting is excellent at temperatures $k_B T \leq \Delta$. The trivial gap monotonously decreases from 46 K to 7.5 K as the bottom gate voltage is decreased from 3 V to -1 V.

3.4.3. Localization of the trivial edge states

By comparison of the Hall bar and Corbino devices, we can see that they show similar gate-tunable resistance behavior at lowest temperatures consistent with the trivial band structure of the bilayer system with sizable bulk gap. However, their conductance minima in the top gate sweeps are orders of magnitude different from each other at any given bottom gate voltage. While the Corbino device exhibits a gap behavior consistent with Arrhenius equation (Fig. 3.7(b)), the Hall bar conductance saturates at low temperatures with a power law increase at elevated temperatures. The temperature behavior of the Hall bar conductance minima is shown in Fig. 3.8. For all bottom gate voltages or equivalently trivial bulk gap sizes, the minimum conductance in top gate sweep starts to increase in power law after a gap-dependent critical temperature below which the conductance is nearly temperature-independent. This behavior, presented in Fig. 3.8, is totally different from activated behavior observed in Corbino disk with merely bulk conduction. Together with the non-local resistance measurements, we can conclude that the transport in the Hall bar device is dominated by trivial edge states in the bulk gap region.

For the purpose of examining the localization of trivial edge modes, we extracted the edge component of the Hall bar conductance in combination with the Corbino measurements. Figure 3.9 illustrates G_{edge} of the Hall bar inside the trivial gap as a function of temperature in the range of 0.2 to 30 K for different bottom gate voltages. G_{edge} is obtained by subtracting the bulk conductance, $G_{bulk} = (W/L)\sigma_{bulk}$, from the total conductance of the Hall bar. The edge conductance displays a distinct temperature behavior, saturates at low temperatures and scales with a power law at higher temperatures. Moreover, a power law with voltage bias is also observed at lowest temperature (inset of Fig. 3.9) in accordance with the theory disscussed in the next paragraph. Here we should note that the edge conductance at low temperatures, where it saturates, is at least two orders of magnitude larger than the bulk conductance. As temperature increases, the bulk and edge conductances increase and become comparable at highest temperatures. These observations verify the dominance of edge conduction in the Hall bar particularly at low temperatures.
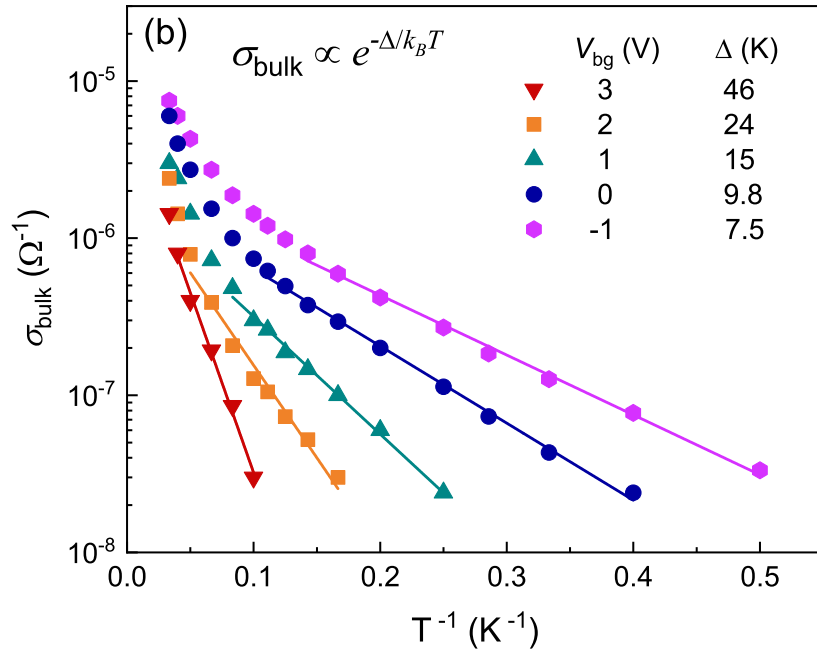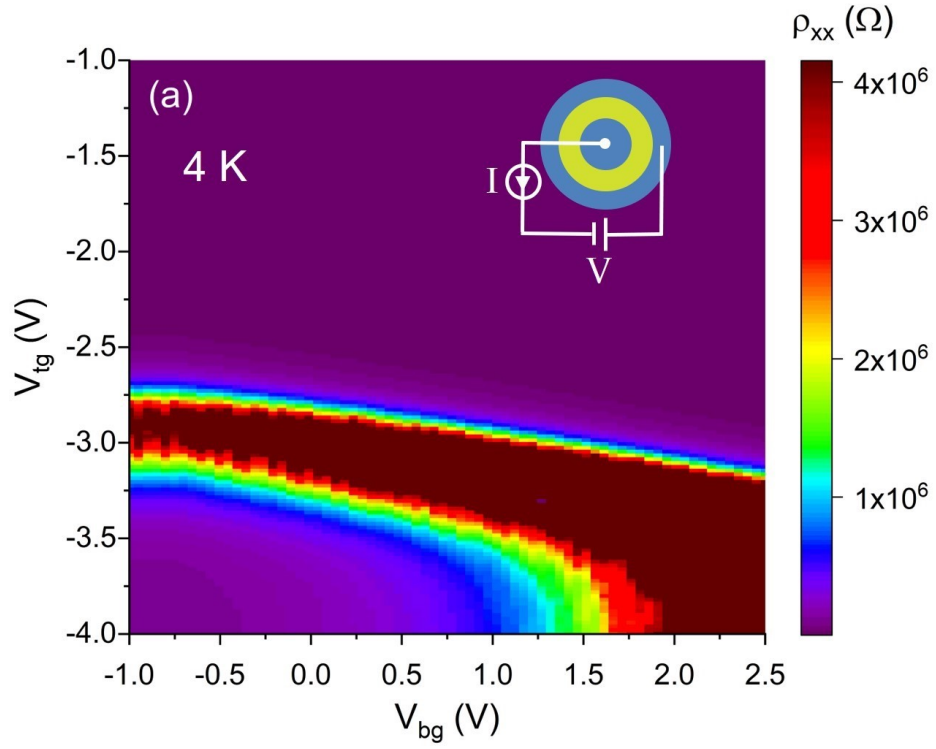
Figure 3.7: (a) The phase diagram of the Corbino disk measured with 100 μV AC bias at $T = 4$ K. (b) Temperature behavior of the minimum bulk conductivity inside the trivial gap for different bottom gate voltages. Solid lines are the fits to the Arrhenius equation giving the corresponding bulk gap for each bottom gate voltage.
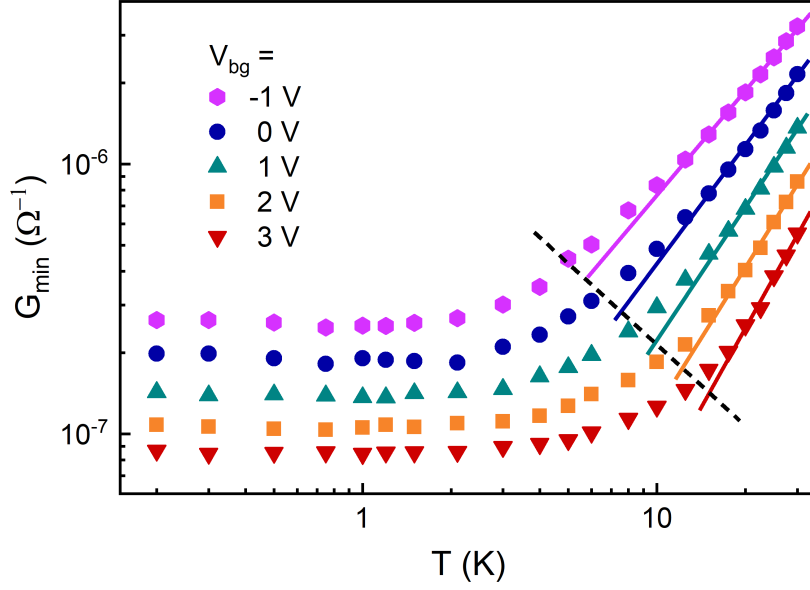
Figure 3.8: Temperature behavior of the Hall bar minimum conductance in top gate sweeps at different bottom gate voltages, characterized by saturation at low temperatures and power law increase at higher temperatures.
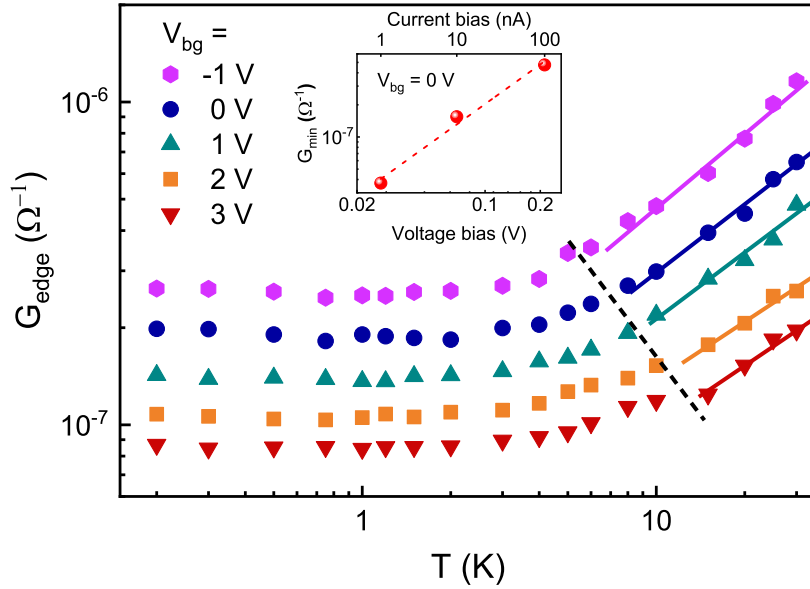
Figure 3.9: Edge component of the Hall bar conductance minima in top gate sweeps as a function of temperature. A power law behavior with an average exponent $\alpha = 0.65 \pm 0.05$ at high temperatures (solid lines) and saturated conductance at low temperatures are observed. Dashed line represents $T = (\gamma/2\pi)V$ with $\gamma = 0.1$. The inset illustrates the power law scaling of the conductance with voltage excitation at lowest temperature, with a corresponding power exponent $\beta = 1.25 \pm 0.02$.

In low dimensional electron systems, disorder commonly causes localization that manifests as an insulating behavior at low bias, V and low temperature, T when system size is considerably larger than the characteristic localization length, ξ. Electron transport in a disordered conductor is governed by variable range hopping (VRH) [65]. In the ohmic regime ($V \ll T$), the conductance is usually described by a stretched exponential behavior with respect to temperature, $G(T) \propto exp[-(T_0/T)^\mu]$, where μ depends on the dimension of the system. On the other hand, in recent years, a Luttinger-liquid-like behavior is observed in transport experiments on one-dimensional systems made from a wide range of materials [66–71]. The observations are characterized by a conductance that varies in a power law with respect to temperature and bias voltage. However, it was shown by numerical analysis that in quasi-1D systems containing large number of channels, the VRH can also reduce to power law described by the following equations [72]:

$$G \propto T^\alpha, \quad T \gg (\gamma/2\pi)V,$$
$$G \propto V^\beta, \quad T \ll (\gamma/2\pi)V,$$

(3.1)

where γ is a material and sample dependent parameter that ranged anywhere from 0.01 to 1 in the experiments. Our analysis of temperature-dependence of bulk and edge conductances is in agreement with the aforementioned theory. At sufficiently low temperatures $T \ll (\gamma/2\pi)V$, the edge conductance is nearly independent of temperature whereas at $T \gg (\gamma/2\pi)V$ it scales as power law (Fig. 3.9). The transition temperatures between the asymptotic saturation and power law behaviors are indicated by dashed line. We conclude a quasi-one-dimensional localization when the Fermi level is tuned inside the normal gap of the system.

3.4.4. Localization length

In the localization regime in a one dimensional electronic system, the conductance exponentially decays with increasing length as long as the system length is larger than the mean free path. We studied the length dependency of the conductance dips in the top gate sweep applied on finger gates of different lengths. It should be noted that the strong suppression of conductance is also observed in edge lengths as short as 1 μm. The dip of longitudinal conductance in top gate sweeps as a function of edge length is shown in Fig. 3.10. Unlike the existing reports on the quasi-linear length-dependent resistance of the edge channels either in trivial or topological phases, here we have a nonlinear depression of conductance as the length increases in agreement with a localization picture. It is well known that in one dimension, nearly all eigenstates of a disordered system are exponentially localized
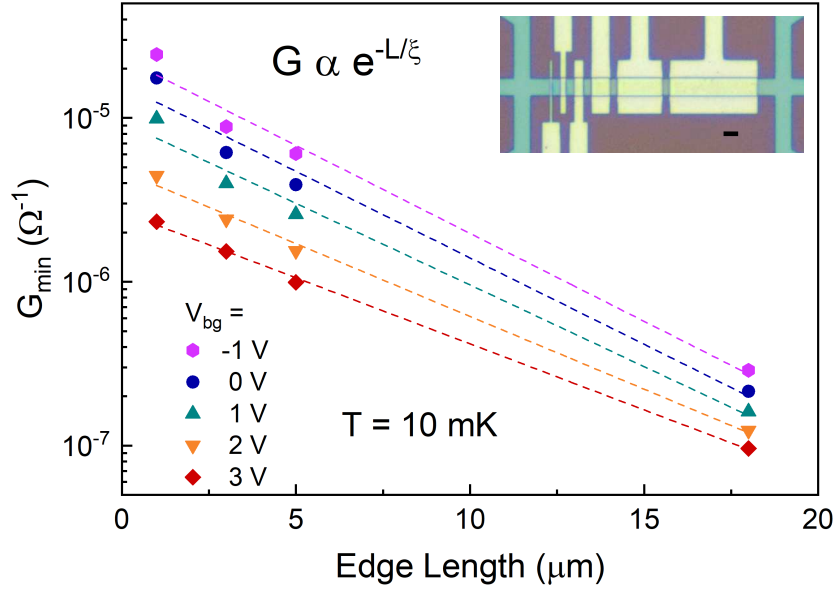
Figure 3.10: The conductance minimum vs edge length measured in the finger gated device. Optical microscope image is shown in the inset, the black scale bar indicates 10 μm length.

at low temperatures. Consequently, the conductance decays in an exponential manner as the length increases. The localization length is obtained as $\xi \approx 4.5 \ \mu m$ which leads to a strong localization even in micron-size edges.

3.5. Conclusion

In summary, we observed that in InAs/GaSb bilayer QW structure trivial edge states are strongly localized when InAs layer is weakly disordered. Our analysis of temperature- and length-dependent edge conduction indicates that silicon atoms that are delta-doped in the InAs layer near the interface of quantum wells are the principal scatterers for e-type carriers as the measured mean free path coincides with the mean spacing between dopants. 2D bulk in the electron band still keeps its high mobility features. The bulk conductivity is characterized as a gapped semiconductor and exponentially diminishes at low temperatures while the conductance due to the edge states prevail in the Hall bar devices. In-depth measurements on Corbino devices and non-local conductivity experiments used to verify the edge states independently. The temperature dependence of the edge states in the non-inverted regime is consistent with the quasi-1D localization; scales by power law at high-T and saturates at low-T. The parameter γ which defines the transition temperature is determined to be 0.1. Furthermore, at high bias regime, the edge conductance enhances in power law with voltage. These are in general agreement with the previous reports on various 1D systems. The conductance of edge states is measured to scale exponentially with length in the finger gate device and the localization length is calculated

26

as 4.5 μm. The elimination of undesired trivial edge conductance in InAs/GaSb system is significant towards the realization of a pure QSH phase with only topologically protected helical edge modes. New structures will be explored to overcome the back gate issues and confirm access to the non-trivial phase.

Chapter 4

SPIN ORBIT INTERACTION

Topological insulators inherently possess strong spin-orbit coupling (SOC). Spin orbit interaction (SOI) together with band inversion are the two main components to form a topological insulator. As a QSHI candidate, the InAs/GaSb bilayer QW has strong spin-orbit coupling which has been subjected to many experimental and theoretical studies.

In this chapter, following an introduction to SOI and its experimental indications, we present magneto-transport study in an InAs/GaSb double quantum well structure in the weak localization regime. The strength of SOI can be identified by the spin-orbit length L_{so} over which the spin of the electron undergoes a full rotation. In diffusive two dimensional systems, where the quantum interference becomes important, the SOI leads to a positive magneto-resistance near zero magnetic field known as the weak anti-localization (WAL), as long as the phase coherence length is larger than spin-orbit length. Otherwise, the dominant phase breaking scatterings results in a weak localization (WL) feature that is a negative magneto-resistance around zero field.

The 2D nature of the transport in our heterostructure is verified by the magnetoresistance study and also the resistance behavior of a Corbino device. As the charge carriers are depleted using a top gate electrode, we observe a crossover from weak anti-localization to weak localization, when the inelastic phase breaking time decreases below spin-orbit characteristic time as a result of enhanced electron-electron interactions at lower carrier concentrations. The same crossover is observed with increasing temperature. The linear temperature behavior of inelastic scattering rate indicates that the dominant phase breaking mechanism in our 2D system is due to electron-electron interaction.

4.1. Introduction

Any crystal material with time reversal and spatial inversion symmetries is spin-degenerate, that is the spin-up and spin-down electrons at a given momentum have the same energy: $E_\uparrow(\vec{k}) = E_\downarrow(\vec{k})$. Breaking either of these symmetries results in lifting the spin degeneracy.

Under magnetic field the time reversal symmetry is broken and the spins split due to Zeeman effect. An asymmetry in the crystal potential can also remove the spin degeneracy even at zero magnetic field B, through the spin-orbit interaction [73, 74]. Indeed, the spin-orbit coupling is a consequence of the electric field which is built up as a result of the asymmetric potential. Analogous to the nucleus electric field, the crystal field generates an effective magnetic field when transforming to the rest frame of the moving electrons. This type of SOC can be in the form of Dresselhaus interaction caused by a bulk inversion asymmetry (BIA) [75] e.g. in zinc blende structures, or Rashba spin-orbit contribution due to structure inversion asymmetry (SIA) of the confinement potential [76–82]. We should note that since the SOI is time-reversal-invariant we still have the Kramers degeneracy i.e. $E_\uparrow(\vec{k}) = E_\downarrow(-\vec{k})$.

A 2DEG in a quantum well can be described by the zeroth order Hamiltonian H_0 with parabolic dispersion in the absence of SOC. The Rashba and Dresselhaus spin-orbit contributions add linear terms in $\vec{k}$ to the Hamiltonian as follows [73, 74]:

$$
\begin{aligned}
H &= H_0 + H_R + H_D \\
&= \frac{\hbar k_\parallel^2}{2m^\star} + \alpha_R \left(\sigma_x k_y - \sigma_y k_x \right) + \beta_D \left(\sigma_x k_x - \sigma_y k_y \right) + \gamma_D \left(\sigma_x k_x k_y^2 - \sigma_y k_y k_x^2 \right),
\end{aligned}
\tag{4.1}
$$

where $k_\parallel = \sqrt{k_x^2 + k_y^2}$ is the momentum parallel to the plane of 2DEG. σ_x and σ_y are the Pauli matrices for the spin components in the plane of 2DEG. α_R, β_D, and γ_D are the Rashba, linear Dresselhaus, and cubic Dresselhaus coefficients, respectively.

The band structure and the confinement of the quantum well influence the Dresselhaus contribution to SOI. In 2D systems, β_D, and γ_D are related by the following equation:

$$
\beta_D = \gamma_D \langle k_z^2 \rangle,
\tag{4.2}
$$

where $\langle k_z^2 \rangle \approx (\pi/d)^2$ is the expectation value of the perpendicular component of momentum in a QW of thickness d. Therefore, a thinner QW would lead to a stronger Dresselhaus effect.

Rashba SOC effect is influenced by the electric field normal to the growth direction, i.e. $\langle E_z \rangle$. This is particularly interesting as the Rashba spin-orbit interaction can be regulated by electrostatic gating.

$$
\alpha_R = \alpha \langle E_z \rangle,
\tag{4.3}
$$
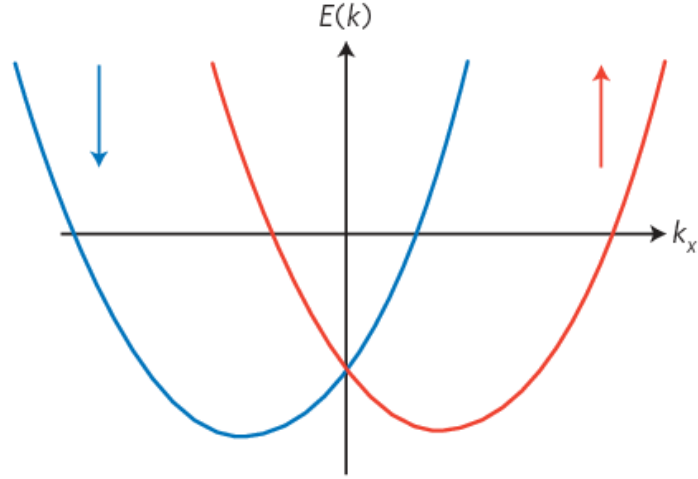
Figure 4.1: Splitting of the spin bands as a consequence of strong spin-orbit interaction.

Disregarding the Dresselhaus cubic term, which has been found negligible in experiments [83–85], the other two terms are linear with respect to in-plane momentum components. This implies that the Hamiltonian in Eq. 4.1 can be rewritten as a combination of two parabola for each spin band. However, as represented in Fig. 4.1, the energy bands are displaced from the origin in opposite ways for the opposite spin polarizations. This zero-field spin splitting gives rise to different carrier densities of the two non-degenerate spins. This leads to a beating pattern in SdH oscillations as we will discuss in more detail later in this chapter.

It is worth to note that the spin splitting due to SOI causes the spin bands to shift in both momentum and energy coordinates, whereas in the case of Zeeman splitting, the spin bands are separated only in the energy axis.

All in all, the spin-orbit interaction leads to a zero-field spin splitting and provides a versatile tool to manipulate the electron spin without an external magnetic field, which is desired for spintronic applications and quantum information technology [6, 7, 86]. For example, classical spin Hall effect (SHE) and its inverse driven by SOI are useful tools for injection and detection of the spin in spintronics [87].

4.2. Experimental signatures of spin-orbit coupling

The SOC has been studied in several low dimensional systems including two-dimensional electron gases (2DEGs), topological insulators, QW heterostructures, semiconducting nanowires, etc. [83–85, 88–104]. A strong SOI can be reflected in magnetoresistance measurements in two different ways. In high mobility systems a beating pattern in Shubnikov-de Haas (SdH) oscillations may be observed as a result of two different SdH frequencies

corresponding to carrier densities of each spin orientation split by SOI [83–85, 96, 101]. On the other hand, in disordered low mobility structures, the SOI can be quantified by the spin dephasing length (L_{so}) which is extracted from low field magnetoresistance measurements where the strong SOC appears as a WAL phenomenon [102]. In the case of Rashba effect, the spin-orbit length is related to the Rashba interaction coefficient via $\alpha_R = \hbar^2/m^\star L_{so}$.

4.2.1. Frequency beating in SdH oscillations

In quantum Hall effect, when a perpendicular magnetic field B is applied to a 2DEG system, the charge carriers condense to discrete energy states. These so-called Landau levels are separated by $\hbar\omega_c \equiv \hbar e B/m^\star$, where $m^\star$ is the electron effective mass. Landau levels are highly degenerate because all zero-field states within an energy range of $\hbar\omega_c$ condense to a single Landau level. The density of states per Landau level n_L is simply equal to the number of flux quanta ($\phi_0 = h/e$) per unit area of the sample within a factor of 2 for double spin degeneracy: $n_L = 2eB/h$. The filling factor at a given field is defined as the total density of the electrons divided by the Landau levels degeneracy n/n_L:

$$\nu = \frac{nh}{2eB}, \tag{4.4}$$

Note that the number of occupied Landau levels under the Fermi level decreases with field while their energy and density of states increase proportional to the magnetic field. As the magnetic field is changed, the Fermi level E_F may lie in between two Landau levels or inside a Landau level. When it is in the middle of a Landau level, the states available for scattering are maximized thus the resistivity ρ_{xx} is maximum. On the other hand, when E_F is situated between Landau levels, a minimum in ρ_{xx} occurs due to lack of available states for scattering.

Hence, at sufficiently low temperatures and high magnetic fields when $\hbar\omega_c \gg k_B T$, the resistance would be almost zero between successive Landau levels and narrowly peaks at transition to the next Landau level. At low fields, however, the resistance ρ_{xx} experiences oscillations, known as Shubnikov-de Haas oscillations, as the Fermi level sweeps between Landau levels. The filling factor or equivalently the number of occupied Landau levels between subsequent peaks is changed by one ($\Delta\nu = 1$). It implies that at a constant electron density the SdH oscillations are periodic in $1/B$ with a frequency $f = \Delta\nu/\Delta(1/B)$. Therefore, from SdH oscillations, one can infer the carrier density for each spin as:

$$n = \frac{fe}{h}, \tag{4.5}$$

Now refering to section 4.1, when we have spin splitting, the carrier density of opposite spins are slightly different. As a result their correspondent SdH frequencies are somewhat different leading to beating patterns in SdH oscillations [83–85]. The strength of SOC can be evaluated by the analysis of SdH beat modulation, though the Zeeman splitting should also be included.

4.2.2. Magnetoresistance in 2D disordered systems with SOC

In disordered metals and semiconductors, the conducting electrons are scattered off impurities or defects. In two dimensions, it is more probable for the electrons to follow self-intersecting trajectories after multiple random elastic scatterings. As represented in Fig. 4.2, an electron can propagate in either of the counterpropagating directions around a closed loop. If the system is invariant under time reversal symmetry, the quantum interference of the electron waves traveling along the time-reversed paths of identical lengths would be constructive as long as individual scatterings preserves the phase coherence. This quantum interference phenomena, that is called *weak localization* (WL) effect, enhances the backscattering probability thus effectively increases the resistivity above the classical terms. A small magnetic field would suppress the constructive interference by breaking the time reversal symmetry, which leads to a positive magnetoconductivity (Fig. 4.2(a)). On the other hand, in the presence of the SOC, the electron's spin rotates continuously in the effective spin-orbit field traveling along the loop. However, the rotation of spin is in the opposite ways for the counterpart paths around the loop thus acquiring different phases. Therefore the partial electron wavefunctions, corresponding to two counter-propagating trajectories, interfere destructively. In this case, the quantum correction to the zero-field conductivity becomes positive. Consequently, upon applying a small magnetic field, the conductivity decreases that is known as the *weak antilocalization* (WAL) effect as shown schematically in Fig. 4.2(b).

The effect of SOI has been widely studied for systems with random potential scattering. In the weak localization limit, the different scattering mechanisms in competition with each other determine the diffusive transport behavior of mesoscopic devices [106–108]. The corresponding scattering rates or equivalently characteristic lengths, including the spin relaxation length L_{so}, can be extracted from low field magnetotransport study of the longitudinal conductivity.
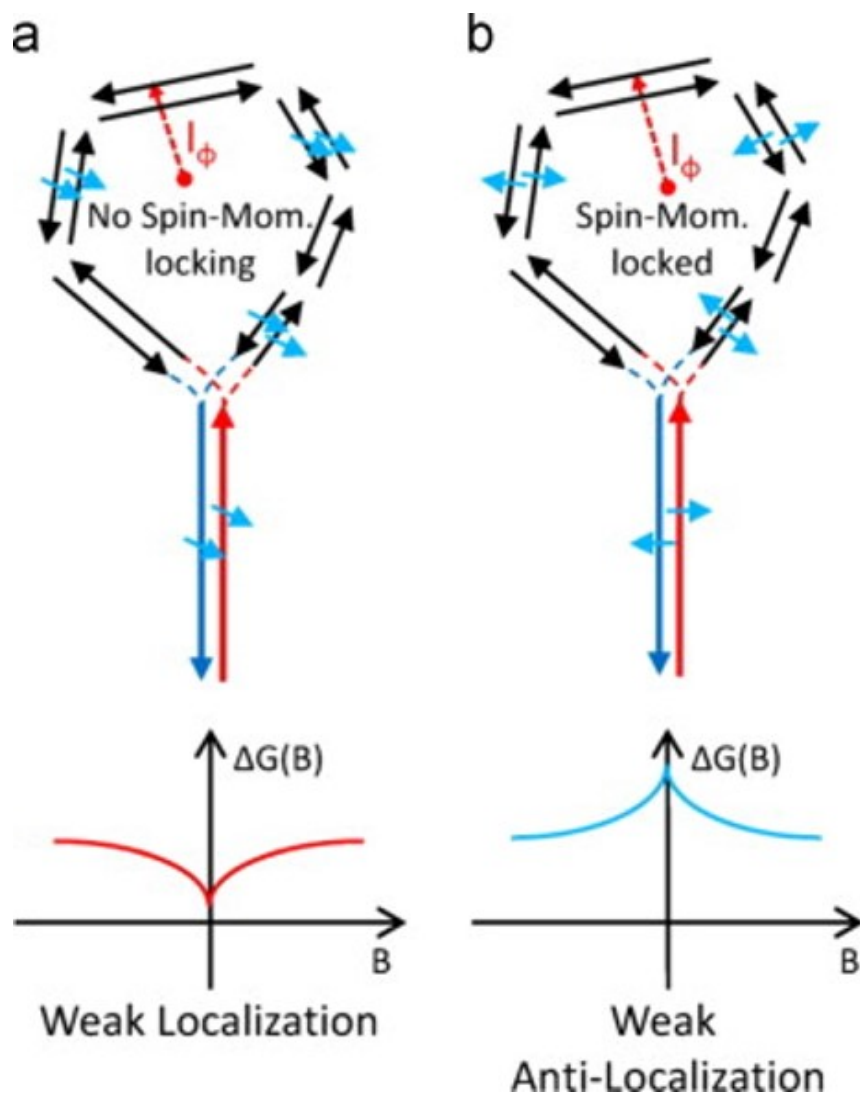
Figure 4.2: Schematic WL and WAL effects. (a) In a spin-degenerate system, the electron waves moving around identical intersecting trajectories interfere constructively thus increase the backscattering probability, i.e. WL phenomenon. (b) The SOC locks the electron spin to its momentum leading to a destructive interference in closed loop time-reversed trajectories. The net difference of the spin rotation between two counter-paths is 2π which results in a π phase difference between the two wavefunctions that is a destructive superposition (WAL effect). Adapted from [105].

The quantum correction to the magnetoconductivity of a 2D system with disorder is well described by Hikami–Larkin–Nagaoka (HLN) interference model [106] which characterizes the WL and WAL phenomena by different scattering mechanisms and their corresponding length scales. The quantum interference correction to the low field magnetoconductivity is given by [106, 107]:

$$\Delta\sigma(B) = -\frac{e^2}{2\pi h}\left\{\psi\left(\frac{B_\phi}{B}+\frac{1}{2}\right) + 2\psi\left(\frac{B_{so}+B_e}{B}+\frac{1}{2}\right) - 3\psi\left(\frac{(4/3)\,B_{so}+B_\phi}{B}+\frac{1}{2}\right)\right.$$
$$\left. - \ln\left(\frac{B_\phi}{B}\right) - 2\ln\left(\frac{B_{so}+B_e}{B}\right) + 3\ln\left(\frac{(4/3)\,B_{so}+B_\phi}{B}\right)\right\}, \qquad (4.6)$$

where $\psi(x)$ is the digamma function and B_i's are the characteristic magnetic fields each corresponds to a different scattering mechanism. By fitting the above equation to the magnetoconductance data with three free parameters we obtained the characteristic fields for inelastic dephasing B_ϕ, spin-orbit B_{so}, and elastic B_e scatterings. One can then obtain the corresponding scattering length via the relation $B_i = \hbar/\left(4eL_i^2\right)$.

4.3. Interaction-induced WAL/WL crossover in a disordered InAs/GaSb heterostructure

In this section, we report a gate-tuned and temperature-induced crossover from WAL to WL. The electron-electron interactions magnify inelastic scattering rate at low densities and high temperatures causing the dephasing length to cross over the SOI length. Applying a top gate voltage, we were able to tune the carrier density and consequently the electron dephasing length L_ϕ due to inelastic scatterings. The enhanced inelastic scattering at lower densities implies electron-electron interactions as the dominant inelastic scattering mechanism. However, the spin-orbit L_{so} and elastic scattering L_e lengths are found nearly independent of V_{tg}. The same crossover is also observed in magnetoconductance measurements at different temperatures. At elevated temperatures, dephasing length L_ϕ decreases below L_{so} crossing over from WAL regime at low temperatures to WL regime at high temperatures.

4.3.1. Wafer structure, devices, and measurement setup

Similar to the heterostructure characterized in Chapter 3 (Wafer A), the heterostructure investigated in this chapter (Wafer B) was grown on a GaAs substrate by molecular beam epitaxy. Following an AlSb buffer layer of about $1\ \mu$m, the bilayer QW structure consist-
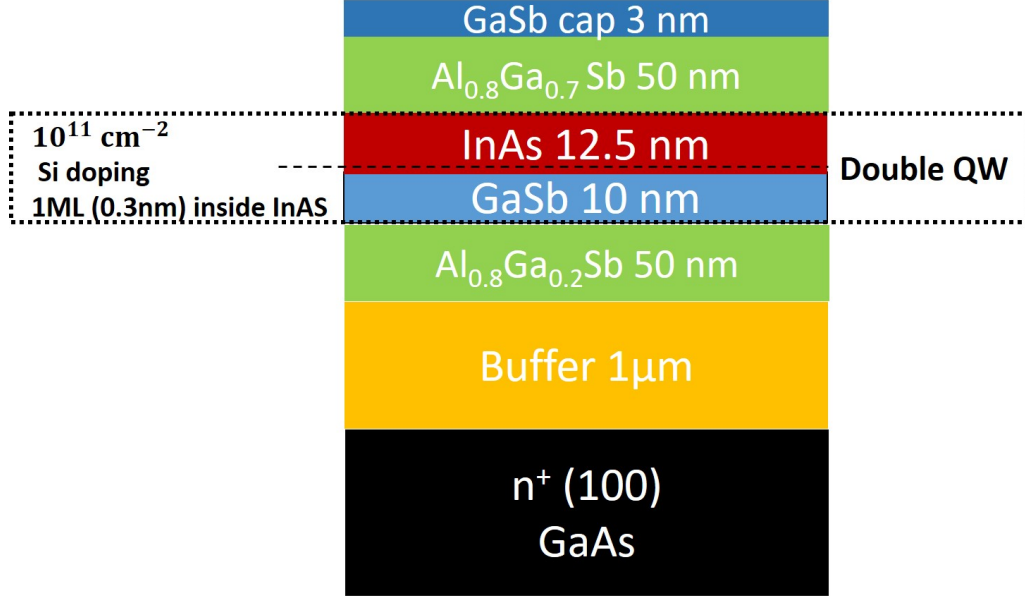
Figure 4.3: Wafer B: Schematic of the heterostructure measured and presented in this chapter with Si delta-dopants inside InAs QW at 1 monolayer distance from the InAs/GaSb interface.

ing of a 12.5 nm InAs layer on a 10nm GaSb layer confined between 50 nm-thick top and bottom AlGaSb barriers was grown. The top barrier was protected from oxidization by a 3nm GaSb cap layer. The structure in this study is also disordered by single layer silicon impurity, however, in different position along the growth direction. In the previous wafer structure[35], the Si atoms with an average density of 10^{11} cm^{-2} were deposited inside the InAs at two atomic monolayer distance from the InAs/GaSb interface, while in the heterostructure B, the silicon particles are placed closer to the interface at only one atomic monolayer distance inside the InAs layer. The details of the wafer material is displayed in Fig. 4.3

A 20×5 μm ($L \times W$) Hall bar device and a Corbino disk which is top-gated by a ring-shaped metal with inner and outer diameters of $r_i = 400$ μm and $r_o = 600$ μm respectively were used in this study. The device mesa was patterned by standard electron beam lithography and defined via chemical wet etching. The etched surfaces are passivated by a 200nm-thick PECVD-grown Si$_3$Ni$_4$ layer which also serves as the dielectric layer separating the top gate Ti/Au electrodes from the heterostructure. The ohmics are made by Ge/Au/Ni metalization without annealing. Transport measurements were performed in a dilution refrigerator with a base temperature of 10 mK using standard lock-in methods with 10 nA current excitation at 7 Hz, unless otherwise stated.
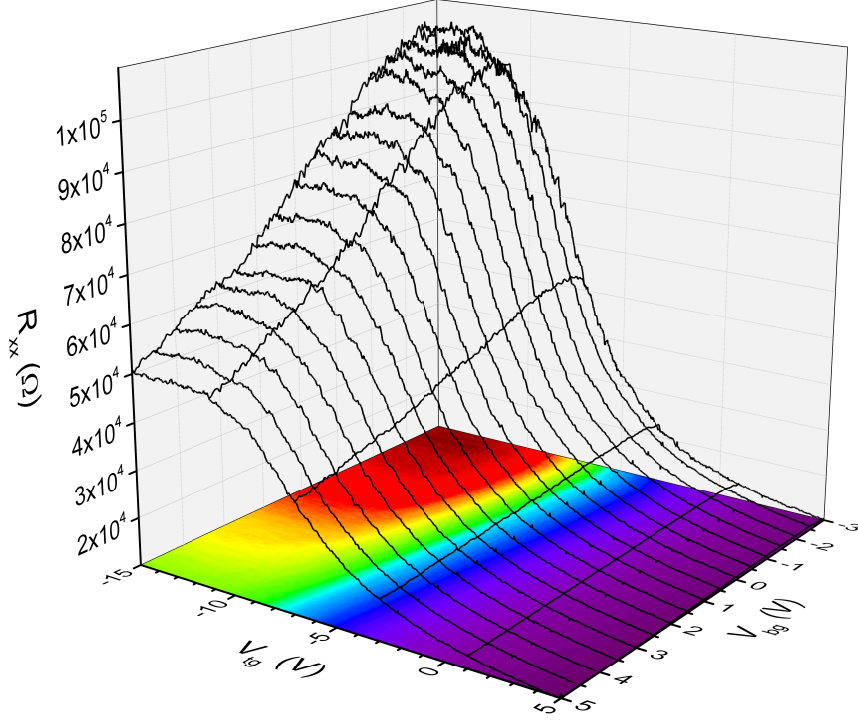
Figure 4.4: Longitudinal resistance of the Hall bar device as a function of V_{tg} and V_{bg} measured at $T = 10$ mK with 10 nA DC current. The sample exhibits semi-metallic behavior in the whole range of top and bottom gate voltages.

4.3.2. Semi-metallic bulk transport

Surprisingly, the wafers A and B have totally different transport properties which is likely due to impurity-induced interfacial effects. In the previous chapter, the bilayer InAs/GaSb heterostructure (Wafer A) exhibited a trivial insulator behavior with a sizable gap using dual gate electrodes. However, for heterostructure B studied in this chapter, the bilayer QW shows a semi-metallic behavior within the whole range of top and bottom gate voltages. The phase diagram of the heterostructure is shown in Fig. 4.4 obtained by sweeping the top gate at different bottom gate voltages. It is noticeable that for all bottom gate voltages, the longitudinal resistance saturates at lowered V_{tg} forming plateaus of different values when $V_{tg} \leq -12\,V$.

The same behavior is observed in the Corbino device which indicates the plateaus are not related to the edge transport behavior.

Although we detected non-local signal, the ratio of local to non-local signal is not more than 5 in the whole range of top gate voltage. This implies that the sample is significantly inhomogeneous resulting in a fictitious non-local resistance. Taking into account these observations we confirm that our heterostructure is in semi-metallic regime with 2D
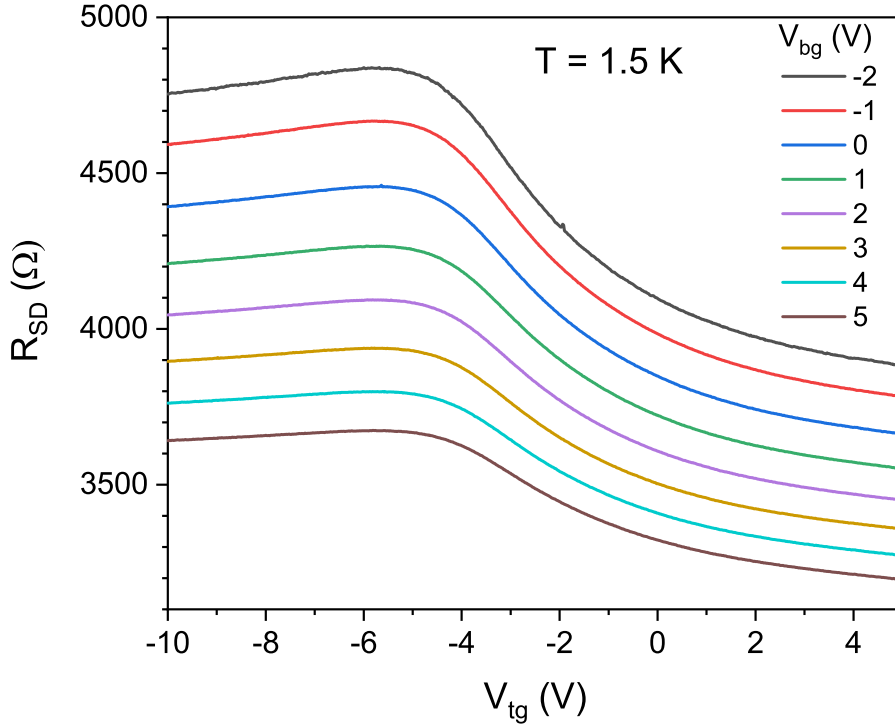
Figure 4.5: Two-terminal resistance of the Corbino device as a function of V_{tg} for different V_{bg} measured with 100 μV AC current between source and drain. The sample exhibits semi-metallic behavior with weak modulation of the resistance.

bulk-dominated diffusive transport. A comprehensive study is required to examine the effect of impurity on these heterostructures. For example, numerical simulations with a variation of disorder strength and position can help to understand how the impurity affects such drastically the transport characteristics of the bilayer InAs/GaSb QWs.

4.3.3. WAL/WL crossover driven by gate voltage

By application of the top gate voltage, a continuous change from WAL to WL regime was observed in the magneto-transport measurements. Figure 4.6(a) illustrates the change of the magnetoconductivity for different top gate voltages from +15 V to -15 V with one volt steps. While at very positive gate voltages the device represents a WAL feature, it gradually evolves to the WL regime when the inelastic dephasing length L_ϕ declines by lowering the top gate voltage and finally crosses over the spin-orbit scattering length L_{so} at $V_{tg} \sim 5\,V$ where the WAL cusp diminishes and the sample shows a WL feature at lower voltages (Fig. 4.6(b)). The most pronounced WAL and WL characteristics at extreme gate voltages are illustrated in Fig. 4.6(b) and 4.6(c), respectively, with perfect fits to the HLN equation. The extracted lengths as functions of top gate voltage are plotted in Fig. 4.6(d). The elastic scattering length and the SO length are nearly independent of gate voltage,
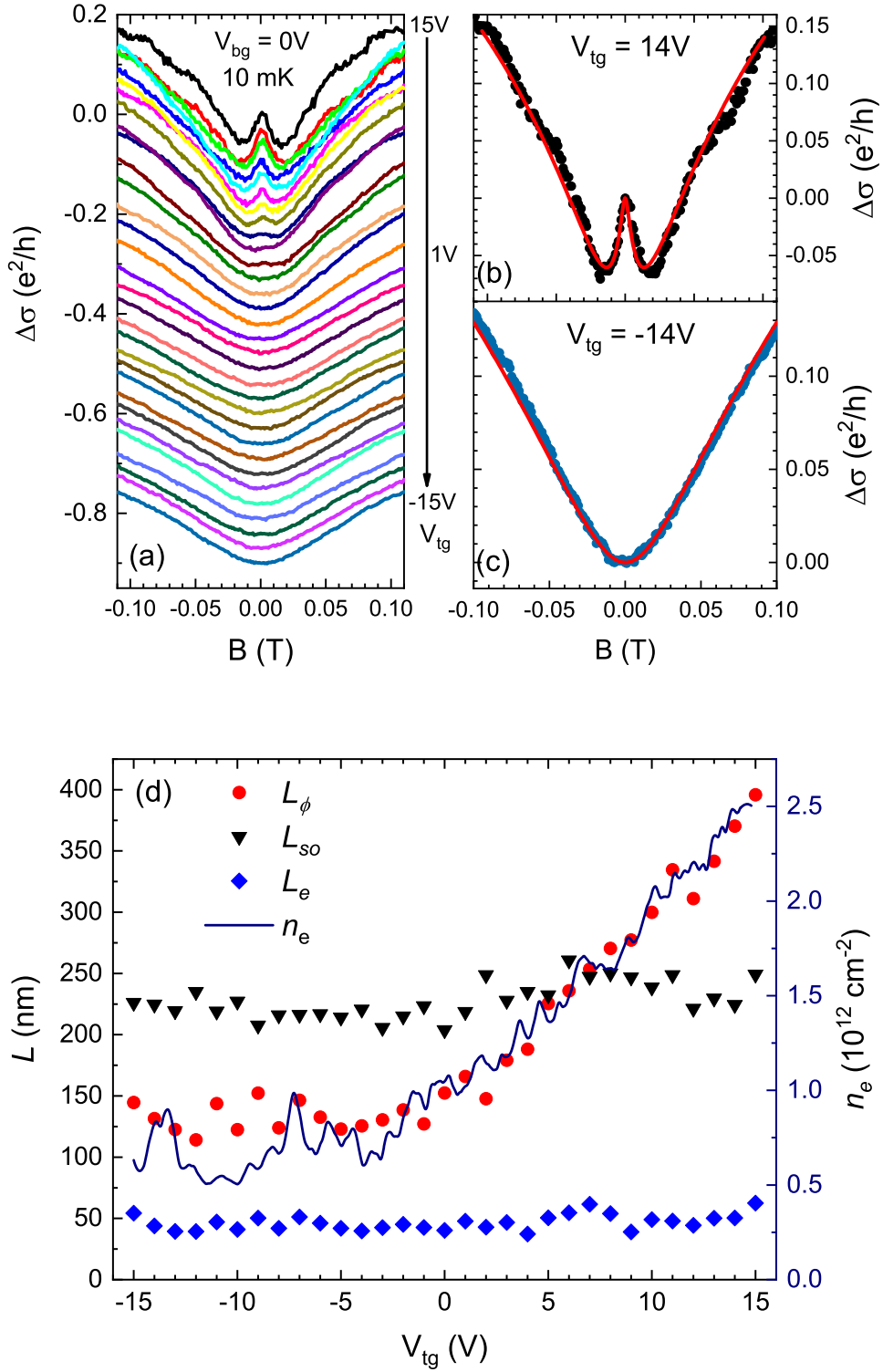
Figure 4.6: Magnetotransport measurements and the characteristic lengths of scatterings. (a) Magnetoconductance correction at different V_{tg}'s where the WAL behavior at $V_{tg} = 15$ V gradually suppresses at lowered gate voltages and converts to WL at $V_{tg} \leq 4$ V. (b) and (c) Magnetoconductance correction at $V_{tg} = +14$ V and $V_{tg} = -14$ V, respectively, showing WAL and WL features with fit curves (red) to the HLN equation. (d) Corresponding scattering lengths as functions of V_{tg} obtained from the HLN fits to the experimental data. The density modulation with V_{tg} is also shown, which is calculated by Hall resistance measurements at constant magnetic fields.

however, it can be seen that the inelastic dephasing length is strongly gate-dependent and decreases by decreasing the gate voltage. To see the correlation between L_ϕ and the carrier density n_e, we plotted the electron density versus top gate voltage in the same graph. It is visible that the dephasing length due to inelastic scattering is linked to the carrier density suggesting that the dominant inelastic process is induced by the electron-electron interactions. It should be noted that the carrier density (n_e) modulation with top gate voltage is not significant within the relatively large voltage range we applied. The electron concentration reduces by less than 3 folds from $n_e = 2.5 \times 10^{12}$ cm^{-2} to about 1×10^{12} cm^{-2}. This indicates that the top gate effective electric field is not sufficient to deplete the QW channel probably due to surface trap states common to the III-V semiconductor interfaces(cite) or impurity-induced charge states inside the bilayer QW. This perhaps explains the gate-independent spin relaxation length L_{so} which is otherwise expected to change with the external electric field via the Rashba SOI [83, 88–96, 101, 102]. In other words, the out of plane electric field in the conducting channel is dominated by the crystal fields rather than the external gate-induced field.

However, for 2D electron systems, the reported strengths of the Rashba effect are markedly different [88–96]. There is a puzzling discrepancy between theoretical expectations and experimental observations of the effect of external electric field on the Rashba SOI such that it is sometimes very weak or even absent [94] and in some experiments far stronger than what theory predicts [95, 96]. For instance in Ref. [95], a weak perpendicular electric field (2 orders of magnitude smaller than the typical built-in electric field) applied to the plane of a 2D hole gas were able to change the Rashba SOI by 20%, whereas in reference to [96], the Rashba coupling was enganced by two folds when the built-in crystal field was changed only by 10% within the range of applied gate voltage. Therefore, the exact effect of gate-induced electric field on the Rashba SOI has been remained ambiguous. Above all, a precise investigation of Rashba effect incorporates the variation of electric field at constant carrier densities because otherwise the effects of density modulation and electric field variation on the amount of Rashba SOI can not be separated.

On the other hand, the electron dephasing length is observed to be a function of carrier concentration. At low temperatures in disordered electronic systems, the phase breaking length is determined by electron-electron collisions in the form of direct Coulomb interaction between conducting electrons or inelastic scattering by the electromagnetic field fluctuations in the potential landscape generated by the moving electrons or by impurities. While the former mechanism does not depend on electron density, the latter is sensitive to the carrier concentration as it changes the potential landscape for cruising

electrons. The scattering time corresponded to the mechanism of e-e interaction with small energy transfer (SET), often referred to as Nyquist scattering, at low temperatures is given by[109, 110]:

$$\tau_N = \frac{2E_F\tau_t}{k_B T \ln{(E_F\tau_t/\hbar)}} \equiv \frac{\hbar g}{k_B T \ln{(g/2)}},$$ (4.7)

where, $E_F = \hbar^2 k_F^2/2m^\star$ is the Fermi energy, $m^\star$ is the electron effective mass, and $\tau_t = \mu m^\star/e$ is the transport time also called mean free time i.e. the time between consecutive scattering events. And g is the dimensionless conductivity in units of e^2/h. The characteristic length are related to their corresponding times via $L_i^2 = D\tau_i$, where D is the electron Diffusion coefficient given by:

$$D = \frac{\hbar^2 k_F^2 \tau_t}{2m^2} \equiv \frac{\hbar g}{2m^\star},$$ (4.8)

Referring to Eq. 4.7, at a given temperature, the Nyquist time τ_N thus the dephasing length decreases at lower charge densities n_e (or equivalently smaller E_F) consistent with our observation of gate-dependent dephasing length. As illustrated in Fig. 4.6(d), we observe that L_ϕ reduces with decreasing electron concentration and saturates when n_e saturates at lowest top gate voltages in agreement with the Nyquist interaction model. Therefore, in the heterostructure of this study, the phase breaking time τ_ϕ is determined by the characteristic time of the electron scattering by electromagnetic fluctuations with small energy transfer that is the Nyquist time ($\tau_\phi \sim \tau_N$).

4.3.4. Temperature-induced WAL/WL crossover

Localization theories predict that inelastic scattering rates magnify at higher temperatures. The temperature dependence of the quantum interference corrections due to electron scatterings is quantified by the time τ_ϕ during which the electron wavefunction remains phase-coherent. In highly interacting two-dimensional electron systems, the phase breaking scattering mechanisms are dominated by Nyquist scattering rate induced by electron-electron interaction given by Eq. 4.7. We conducted the temperature study of the magnetoconductance at $V_{tg} = +14V$ where a prominent WAL behavior is observed at lowest temperatures which indicates that the elastic and spin-orbit scatterings are dominant over inelastic phase breaking interactions. As expected, the inelastic scattering mechanisms strengthen at increased temperatures leading to a transition from WAL to WL regime when the L_ϕ reduces below the L_{so}. The temperature study of the magne-
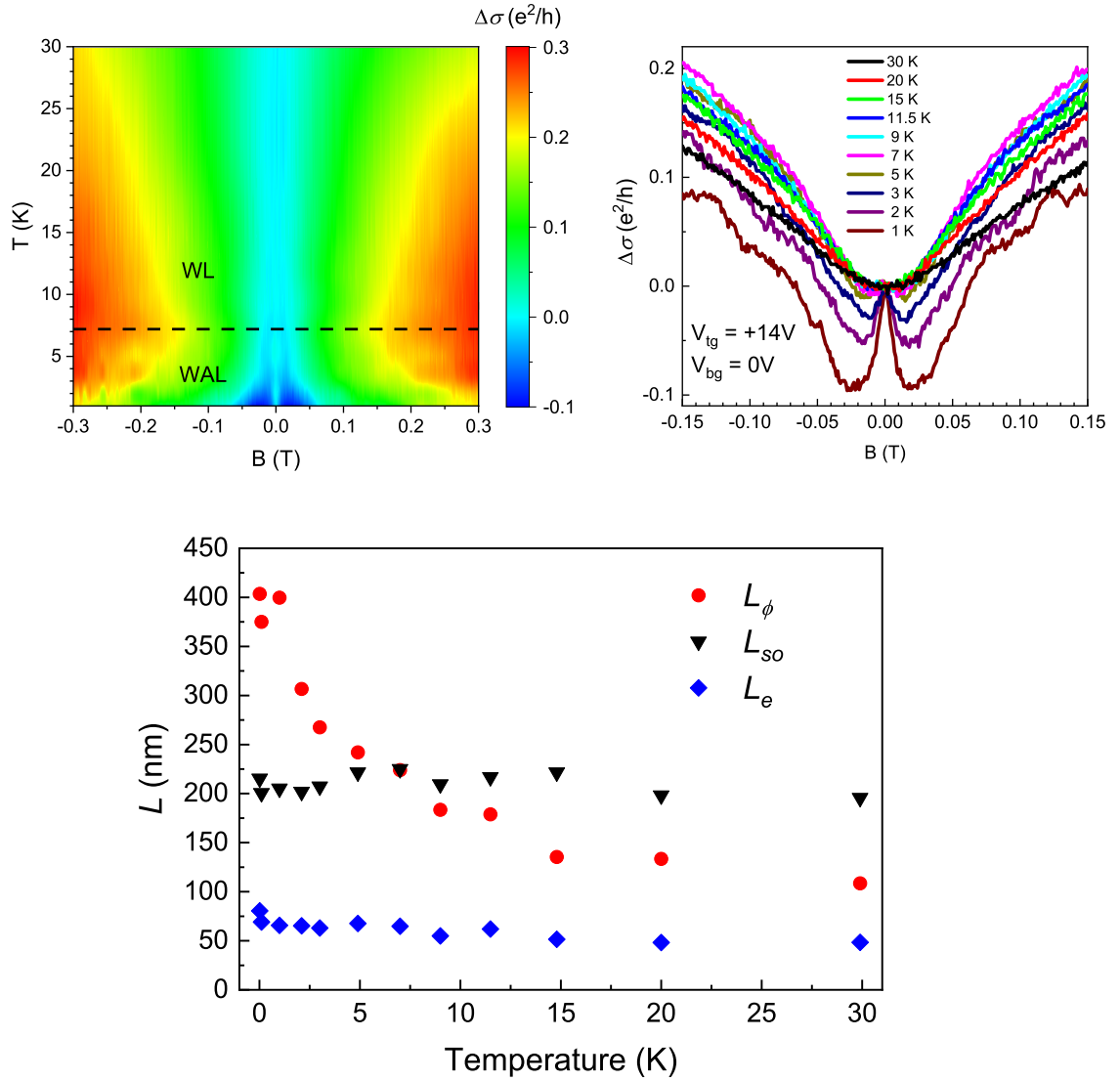
Figure 4.7: Temperature-induced WAL/WL crossover. (a) Magnetoconductance quantum correction measured at different temperatures when $V_{bg} = 0$ V and $V_{tg} = +14$ V. (b) The inelastic dephasing length L_ϕ, spin relaxation length L_{so}, and elastic mean free path L_e as functions of temperature obtained from theoretical fits to the measurements shown in (a).
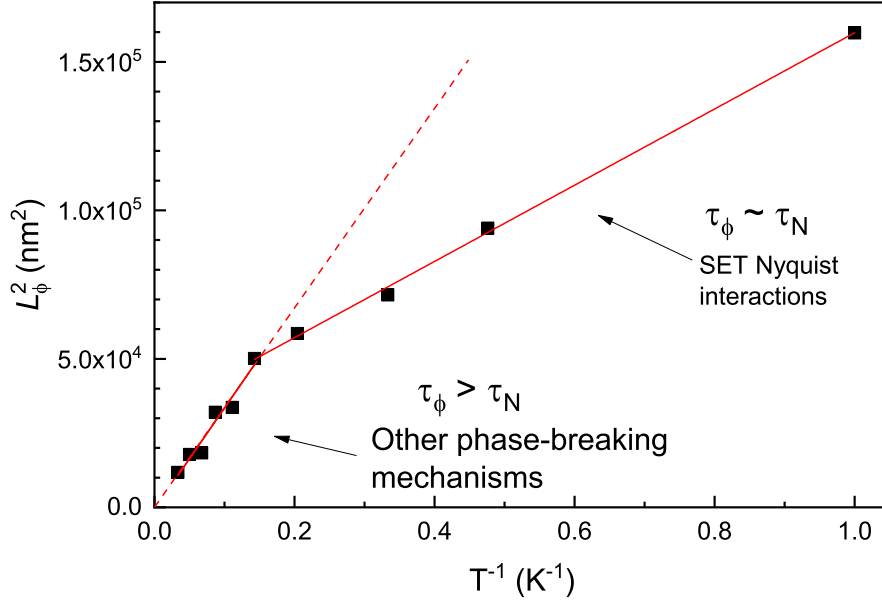
Figure 4.8: $L_\phi^2 \propto \tau_\phi$ shows a linear behavior with inverse temperature (T^{-1}) as expected for inelastic phase breaking scatterings induced by e-e interactions. At low temperatures the SET Nyquist scattering is dominated while at higher temperatures the effective dephasing time is larger than the Nyquist time.

toconductance correction is indicated in Fig. 4.7. The positive cusp of the conductance correction around zero field, that characterizes the WAL, gradually suppresses by increasing the temperature until it enters the WL regime at $T \approx 7$ K where the crossover occurs (Fig. 4.7a). The extracted characteristic lengths which quantifies the crossover are shown in Fig. 4.7b where L_e and L_{so} are insensitive to temperature. Consistent with Eq. 4.7, L_ϕ, which is here equivalent to L_N, decreases with rising temperature. As illustrated in Fig. 4.8, the square of the dephasing length ($L_\phi^2 \propto \tau_N$) is linearly proportional to the inverse temperature. However, the slopes in the WL and WAL regimes are different. At sufficiently low temperatures ($T \leq 7$ K), where the WAL effect is dominant, the slope of the fit line is $1.28 \, (\pm 0.03) \times 10^{-13}$ m^{2}K. On the other hand, substituting all the numbers (assuming the effective mass as $m = 0.04 \, m_e$ [83]) in equation 4.7, which is valid for low temperatures, we obtain a slope of $\approx 1.25 \times 10^{-13}$ m^{2}K which is in perfect agreement with the line slope for WAL (low temperature) regime in Fig. 4.8. At higher temperatures, however, in the WL regime, the slope at which the dephasing length (the Nyquist scattering rate) decreases (increases) with temperature is higher (lower) than that for low temperature regime. The slope of the fit line for $T \geq 7$K is $3.4 \, (\pm 0.4) \times 10^{-13}$ m^{2}K more than two fold larger than that for lower temperatures. At elevated temperatures, the inelastic dephasing mechanisms may deviate from small energy transfer Nyquist interac-

tions due to thermal excitations when the larger energy transfer collisions may play the dominant role. Indeed the phase breaking electron-electron interactions reduces at higher temperatures and the inelastic dephasing rate τ_ϕ^{-1} is decreased by the logarithmic factor in Eq. 4.7 [109].

4.4. Conclusion

In conclusion, we observed an interaction-induced crossover between the WAL and WL phenomena in our intentionally disordered InAs/GaSb bilayer QW structure driven by top gate voltage and temperature. The heterostructure with Si delta-doped atoms near the interface of electron and hole QWs demonstrates WAL feature in magnetoconductance measurements at high carrier densities at lowest temperatures as an evidence for strong SOI. Using the HLN model, we obtained the gate and temperature dependences of the characteristic scattering lengths corresponding to three different scattering mechanisms. The elastic scattering length is found as $L_e \sim 50$ nm which is consistent with the mean spacing between Si dopants of ~ 30 nm. It is almost independent of gate voltage and temperature, which indicates the short range scattering induced by impurity or interface roughness is dominant. The SO scattering length also shows no dependence on temperature and gate voltage. We believe that the effective gate-induced electric field is reduced by impurity and trap states leading to a gate-independent L_{so}. The only parameter responsible for the temperature and gate-driven crossover is the electron dephasing length L_ϕ which changes the magnetotransport behavior when it crosses over L_{so} with an indication of enhanced $e - e$ interactions at lower temperatures and charge concentrations. The temperature and gate dependent analysis of the inelastic phase breaking length indicates that the Nyquist scattering, characterized by electron-electron interactions with SET, is the dominant dephasing mechanism at low temperatures where the spin-orbit scattering is still governing the magneto-conductance behavior with a WAL feature. At higher temperatures the inelastic scattering takes over the SO interaction thus leading to the WL effect. At the same time, the dephasing time increases above the Nyquist time meaning that the Nyquist interactions suppressed at higher temperatures and other inelastic processes with larger energy transfer becomes important.

Chapter 5

OUTLOOK

In this thesis we studied the trivial regime of InAs/GaSb composite Qws in the presence of silicon disorder. Through study of three wafer heterostructures, we showed that one atomic difference in the location of impurity with respect to the InAs/GaSb interface layer, may lead to a significant difference in electronic properties and therefore the transport behavior.

The trivial edge states are mainly caused by InAs electron band bending at the edges of the sample and therefore are n-type. When the band bending is comparable to the gap size, it provides trivial edge channels in parallel to bulk conduction. Introducing disorder in InAs layer remote from the interface between InAs and GaSb (at two atomic layer distance), we could localize the trivial edge carriers.

When the silicon atoms are deposited closer to the interface at one atomic layer distance inside the InAs layer, they produce stronger potential fluctuations probably due to reduced screening effects. In this case the strong fluctuations in potential landscape would effectively close the bulk gap if there is any. In fact, the observation of a 2D semi-metallic transport supports the argument. The electron mobility was reduced by an order of magnitude indicating an increased bulk scattering. Moreover, the segregation of Si atoms towards the interface may not be excluded, though we can not testify.

Using a GaSb substrate instead of GaAs, we could gain a richer phase diagram beyond the trivial band regime. The reduced mismatch between the GaSb substrate and the epitaxial layers minimizes the crystal defects and disorders growing towards the active QW channels. This improves the bottom gate performance by reducing the current leakage and also the required dielectric buffer thickness grown between substrate and double QWs. Placing the silicon impurities inside the GaSb QW leads to a reduced localization effect on trivial edge states, but still preserves the normal gap. The inverted regime could not be studied in this thesis and is a subject our future work.

In future experiments, we are planning to explore the inverted band regime and search for signatures of QSHE. We will try to reduce the gate current leakage so that we can ap-

ply larger gate voltages and therefore examine the transport in different phases. We also aim to get a deeper understanding of the role of silicon impurity in our heterostructures by comparison of transport measurements on these three wafers in identical sample sizes and geometries. We also would like to quantify the electron-hole coupling which is critical for their hybridization and therefore inverted gap formation. The possible effect of silicon disorder on the coupling strength is also worth to study. For this purpose we need to somehow probe the interlayer charge transfer via making electric contacts to the electron and hole layers individually. At last but not least, we will study the hyperfine interaction between the spin-polarized edge carriers and the nuclear spins with the motivation by Ref.[9]. The possible energy storage as the nuclear spins polarization and the work extraction induced by a reverse effect would be interesting for realization of a quantum engine.

Bibliography

[1] M. Z. Hasan and C. L. Kane, "Colloquium: Topological insulators," *Rev. Mod. Phys.*, vol. 82, pp. 3045–3067, Nov 2010.

[2] C. L. Kane and E. J. Mele, "Quantum spin hall effect in graphene," *Phys. Rev. Lett.*, vol. 95, p. 226801, 2005.

[3] B. A. Bernevig, T. L. Hughes, and S.-C. Zhang, "Quantum spin hall effect and topological phase transition in hgte quantum wells," *Science*, vol. 314, no. 5806, pp. 1757–1761, 2006.

[4] J. Maciejko, T. L. Hughes, and S.-C. Zhang, "The quantum spin hall effect," *Annual Review of Condensed Matter Physics*, vol. 2, no. 1, pp. 31–53, 2011.

[5] M. König, H. Buhmann, L. W. Molenkamp, T. Hughes, C.-X. Liu, X.-L. Qi, and S.-C. Zhang, "The quantum spin Hall effect: Theory and experiment," *Journal of the Physical Society of Japan*, vol. 77, no. 3, p. 031007, 2008.

[6] I. Žutić, J. Fabian, and S. Das Sarma, "Spintronics: Fundamentals and applications," *Rev. Mod. Phys.*, vol. 76, pp. 323–410, Apr 2004.

[7] X.-L. Qi and S.-C. Zhang, "Topological insulators and superconductors," *Rev. Mod. Phys.*, vol. 83, pp. 1057–1110, Oct 2011.

[8] C. Nayak, S. H. Simon, A. Stern, M. Freedman, and S. Das Sarma, "Non-abelian anyons and topological quantum computation," *Rev. Mod. Phys.*, vol. 80, pp. 1083–1159, Sep 2008.

[9] A. M. Bozkurt, B. Pekerten, and İ. Adagideli, "Work extraction and landauer's principle in a quantum spin hall device," *Physical Review B*, vol. 97, no. 24, p. 245414, 2018.

[10] M. König, S. Wiedmann, C. Brüne, A. Roth, H. Buhmann, L. W. Molenkamp, X.-L. Qi, and S.-C. Zhang, "Quantum spin hall insulator state in hgte quantum wells," *Science*, vol. 318, no. 5851, pp. 766–770, 2007.

[11] A. Roth, C. Brüne, H. Buhmann, L. W. Molenkamp, J. Maciejko, X.-L. Qi, and S.-C. Zhang, "Nonlocal transport in the quantum spin hall state," *Science*, vol. 325, no. 5938, pp. 294–297, 2009.

[12] C. Liu, T. L. Hughes, X.-L. Qi, K. Wang, and S.-C. Zhang, "Quantum spin hall effect in inverted type-ii semiconductors," *Phys. Rev. Lett.*, vol. 100, p. 236601, Jun 2008.

[13] M. Altarelli, "Electronic structure and semiconductor-semimetal transition in inas-gasb superlattices," *Phys. Rev. B*, vol. 28, pp. 842–845, Jul 1983.

[14] Y. Naveh and B. Laikhtman, "Band-structure tailoring by electric field in a weakly coupled electron-hole system," *Applied Physics Letters*, vol. 66, no. 15, pp. 1980–1982, 1995.

[15] I. Knez, R.-R. Du, and G. Sullivan, "Evidence for helical edge modes in inverted InAs/GaSb quantum wells," *Phys. Rev. Lett.*, vol. 107, p. 136603, Sep 2011.

[16] I. Knez, R.-R. Du, and G. Sullivan, "Andreev reflection of helical edge modes in InAs/GaSb quantum spin hall insulator," *Phys. Rev. Lett.*, vol. 109, p. 186603, Oct 2012.

[17] K. Suzuki, Y. Harada, K. Onomitsu, and K. Muraki, "Edge channel transport in the inas/gasb topological insulating phase," *Phys. Rev. B*, vol. 87, p. 235311, Jun 2013.

[18] I. Knez, C. T. Rettner, S.-H. Yang, S. S. P. Parkin, L. Du, R.-R. Du, and G. Sullivan, "Observation of edge transport in the disordered regime of topologically insulating InAs/GaSb quantum wells," *Phys. Rev. Lett.*, vol. 112, p. 026602, Jan 2014.

[19] F. Nichele, A. N. Pal, P. Pietsch, T. Ihn, K. Ensslin, C. Charpentier, and W. Wegscheider, "Insulating state and giant nonlocal response in an InAs/GaSb quantum well in the quantum hall regime," *Phys. Rev. Lett.*, vol. 112, p. 036802, Jan 2014.

[20] I. Knez, C. T. Rettner, S.-H. Yang, S. S. P. Parkin, L. Du, R.-R. Du, and G. Sullivan, "Observation of edge transport in the disordered regime of topologically insulating InAs/GaSb quantum wells," *Phys. Rev. Lett.*, vol. 112, p. 026602, Jan 2014.

[21] E. M. Spanton, K. C. Nowack, L. Du, G. Sullivan, R.-R. Du, and K. A. Moler, "Images of edge current in InAs/GaSb quantum wells," *Phys. Rev. Lett.*, vol. 113, p. 026804, Jul 2014.

[22] L. Du, I. Knez, G. Sullivan, and R.-R. Du, "Robust helical edge transport in gated InAs/GaSb bilayers," *Phys. Rev. Lett.*, vol. 114, p. 096802, Mar 2015.

[23] F. Qu, A. J. A. Beukman, S. Nadj-Perge, M. Wimmer, B.-M. Nguyen, W. Yi, J. Thorp, M. Sokolich, A. A. Kiselev, M. J. Manfra, C. M. Marcus, and L. P. Kouwenhoven, "Electric and magnetic tuning between the trivial and topological phases in inas/gasb double quantum wells," *Phys. Rev. Lett.*, vol. 115, p. 036803, Jul 2015.

[24] V. S. Pribiag, A. J. A. Beukman, F. Qu, M. C. Cassidy, C. Charpentier, W. Wegscheider, and L. P. Kouwenhoven, "Edge-mode superconductivity in a two-dimensional topological insulator," *Nature Nanotechnology*, vol. 10, p. 593, May 2015.

[25] T. Li, P. Wang, H. Fu, L. Du, K. A. Schreiber, X. Mu, X. Liu, G. Sullivan, G. A. Csáthy, X. Lin, and R.-R. Du, "Observation of a helical luttinger liquid in InAs/GaSb quantum spin hall edges," *Phys. Rev. Lett.*, vol. 115, p. 136804, Sep 2015.

[26] M. Karalic, S. Mueller, C. Mittag, K. Pakrouski, Q. Wu, A. A. Soluyanov, M. Troyer, T. Tschirky, W. Wegscheider, K. Ensslin, and T. Ihn, "Experimental signatures of the inverted phase in inas/gasb coupled quantum wells," *Phys. Rev. B*, vol. 94, p. 241402, Dec 2016.

[27] F. Nichele, H. J. Suominen, M. Kjaergaard, C. M. Marcus, E. Sajadi, J. A. Folk, F. Qu, A. J. A. Beukman, F. K. de Vries, J. van Veen, S. Nadj-Perge, L. P. Kouwenhoven, B.-M. Nguyen, A. A. Kiselev, W. Yi, M. Sokolich, M. J. Manfra, E. M. Spanton, and K. A. Moler, "Edge transport in the trivial phase of inas/gasb," *New Journal of Physics*, vol. 18, no. 8, p. 083005, 2016.

[28] B.-M. Nguyen, A. A. Kiselev, R. Noah, W. Yi, F. Qu, A. J. A. Beukman, F. K. de Vries, J. van Veen, S. Nadj-Perge, L. P. Kouwenhoven, M. Kjaergaard, H. J. Suominen, F. Nichele, C. M. Marcus, M. J. Manfra, and M. Sokolich, "Decoupling edge versus bulk conductance in the trivial regime of an InAs/GaSb double quantum well using corbino ring geometry," *Phys. Rev. Lett.*, vol. 117, p. 077701, Aug 2016.

[29] W. Yu, V. Clericò, C. H. Fuentevilla, X. Shi, Y. Jiang, D. Saha, W. K. Lou, K. Chang, D. H. Huang, G. Gumbs, D. Smirnov, C. J. Stanton, Z. Jiang, V. Bellani, Y. Meziani, E. Diez, W. Pan, S. D. Hawkins, and J. F. Klem, "Anomalously

large resistance at the charge neutrality point in a zero-gap InAs/GaSb bilayer," *New Journal of Physics*, vol. 20, p. 053062, may 2018.

[30] B. Shojaei, A. P. McFadden, M. Pendharkar, J. S. Lee, M. E. Flatté, and C. J. Palmstrøm, "Materials considerations for forming the topological insulator phase in inas/gasb heterostructures," *Phys. Rev. Materials*, vol. 2, p. 064603, Jun 2018.

[31] S. S. Krishtopenko, S. Ruffenach, F. Gonzalez-Posada, G. Boissier, M. Marcinkiewicz, M. A. Fadeev, A. M. Kadykov, V. V. Rumyantsev, S. V. Morozov, V. I. Gavrilenko, C. Consejo, W. Desrat, B. Jouault, W. Knap, E. Tournié, and F. Teppe, "Temperature-dependent terahertz spectroscopy of inverted-band three-layer inas/gasb/inas quantum well," *Phys. Rev. B*, vol. 97, p. 245419, Jun 2018.

[32] X. Wu, W. Lou, K. Chang, G. Sullivan, and R.-R. Du, "Resistive signature of excitonic coupling in an electron-hole double layer with a middle barrier," *Phys. Rev. B*, vol. 99, p. 085307, Feb 2019.

[33] M. Karalic, C. Mittag, S. Mueller, T. Tschirky, W. Wegscheider, K. Ensslin, T. Ihn, and L. Glazman, "Phase slips and parity jumps in quantum oscillations of inverted inas/gasb quantum wells," *Phys. Rev. B*, vol. 99, p. 201402, May 2019.

[34] D. Xiao, C.-X. Liu, N. Samarth, and L.-H. Hu, "Anomalous quantum oscillations of interacting electron-hole gases in inverted type-ii $\mathrm{InAs/GaSb}$ quantum wells," *Phys. Rev. Lett.*, vol. 122, p. 186802, May 2019.

[35] V. Sazgari, G. Sullivan, and I. I. Kaya, "Localization of trivial edge states in inas/gasb composite quantum wells," *Phys. Rev. B*, vol. 100, p. 041404, Jul 2019.

[36] K. Suzuki, Y. Harada, K. Onomitsu, and K. Muraki, "Gate-controlled semimetal-topological insulator transition in an inas/gasb heterostructure," *Phys. Rev. B*, vol. 91, p. 245309, Jun 2015.

[37] F. m. c. Couëdo, H. Irie, K. Suzuki, K. Onomitsu, and K. Muraki, "Single-edge transport in an inas/gasb quantum spin hall insulator," *Phys. Rev. B*, vol. 94, p. 035301, Jul 2016.

[38] C. Charpentier, S. Fält, C. Reichl, F. Nichele, A. Nath Pal, P. Pietsch, T. Ihn, K. Ensslin, and W. Wegscheider, "Suppression of bulk conductivity in inas/gasb broken gap composite quantum wells," *Applied Physics Letters*, vol. 103, no. 11, p. 112102, 2013.

[39] S. Mueller, A. N. Pal, M. Karalic, T. Tschirky, C. Charpentier, W. Wegscheider, K. Ensslin, and T. Ihn, "Nonlocal transport via edge states in inas/gasb coupled quantum wells," *Phys. Rev. B*, vol. 92, p. 081303, Aug 2015.

[40] D.-H. Xu, J.-H. Gao, C.-X. Liu, J.-H. Sun, F.-C. Zhang, and Y. Zhou, "Localized in-gap states and quantum spin hall effect in si-doped inas/gasb quantum wells," *Phys. Rev. B*, vol. 89, p. 195104, May 2014.

[41] C. Ndebeka-Bandou and J. Faist, "Disorder effects in inas/gasb topological insulator candidates," *Phys. Rev. B*, vol. 95, p. 045107, Jan 2017.

[42] S. Mueller, C. Mittag, T. Tschirky, C. Charpentier, W. Wegscheider, K. Ensslin, and T. Ihn, "Edge transport in inas and inas/gasb quantum wells," *Phys. Rev. B*, vol. 96, p. 075406, Aug 2017.

[43] K. v. Klitzing, G. Dorda, and M. Pepper, "New method for high-accuracy determination of the fine-structure constant based on quantized hall resistance," *Physical Review Letters*, vol. 45, no. 6, p. 494, 1980.

[44] M. E. Cage, K. Klitzing, A. Chang, F. Duncan, M. Haldane, R. Laughlin, A. Pruisken, and D. Thouless, *The quantum Hall effect*. Springer Science & Business Media, 2012.

[45] C. L. Kane and E. J. Mele, "Z_2 topological order and the quantum spin Hall effect," *Phys. Rev. Lett.*, vol. 95, p. 146802, 2005.

[46] H. Buhmann, "The quantum spin hall effect," *Journal of Applied Physics*, vol. 109, no. 10, p. 102409, 2011.

[47] M. König, "Spin-related transport phenomena in hgte-based quantum well structures," 2007.

[48] H. Min, J. Hill, N. A. Sinitsyn, B. Sahu, L. Kleinman, and A. H. MacDonald, "Intrinsic and rashba spin-orbit interactions in graphene sheets," *Physical Review B*, vol. 74, no. 16, p. 165310, 2006.

[49] Y. Yao, F. Ye, X.-L. Qi, S.-C. Zhang, and Z. Fang, "Spin-orbit gap of graphene: First-principles calculations," *Physical Review B*, vol. 75, no. 4, p. 041401, 2007.

[50] S. Wu, V. Fatemi, Q. D. Gibson, K. Watanabe, T. Taniguchi, R. J. Cava, and P. Jarillo-Herrero, "Observation of the quantum spin hall effect up to 100 kelvin in a monolayer crystal," *Science*, vol. 359, no. 6371, pp. 76–79, 2018.

[51] H. Kroemer, "The 6.1 a family (inas, gasb, alsb) and its heterostructures: a selective review," *Physica E: Low-dimensional Systems and Nanostructures*, vol. 20, no. 3-4, pp. 196–203, 2004.

[52] Y. Naveh and B. Laikhtman, "Band-structure tailoring by electric field in a weakly coupled electron-hole system," *Applied physics letters*, vol. 66, no. 15, pp. 1980–1982, 1995.

[53] J. K. Asbóth, L. Oroszlány, and A. Pályi, "A short course on topological insulators," *Lecture notes in physics*, vol. 919, 2016.

[54] C. Mittag, M. Karalic, S. Mueller, T. Tschirky, W. Wegscheider, O. Nazarenko, M. V. Kovalenko, T. Ihn, and K. Ensslin, "Passivation of edge states in etched inas sidewalls," *Applied Physics Letters*, vol. 111, no. 8, p. 082101, 2017.

[55] D. á. Tsui, "Observation of surface bound state and two-dimensional energy band by electron tunneling," *Physical review letters*, vol. 24, no. 7, p. 303, 1970.

[56] M. Noguchi, K. Hirakawa, and T. Ikoma, "Intrinsic electron accumulation layers on reconstructed clean inas (100) surfaces," *Physical review letters*, vol. 66, no. 17, p. 2243, 1991.

[57] L. Olsson, C. Andersson, M. Håkansson, J. Kanski, L. Ilver, and U. O. Karlsson, "Charge accumulation at inas surfaces," *Physical review letters*, vol. 76, no. 19, p. 3626, 1996.

[58] C. Gatzke, S. Webb, K. Fobelets, and R. Stradling, "In situ raman spectroscopy of the selective etching of antimonides in gasb/alsb/inas heterostructures," *Semiconductor science and technology*, vol. 13, no. 4, p. 399, 1998.

[59] R. Chaghi, C. Cervera, H. Aït-Kaci, P. Grech, J. Rodriguez, and P. Christol, "Wet etching and chemical polishing of inas/gasb superlattice photodiodes," *Semiconductor Science and Technology*, vol. 24, no. 6, p. 065010, 2009.

[60] E. A. Plis, M. N. Kutty, and S. Krishna, "Passivation techniques for inas/gasb strained layer superlattice detectors," *Laser & Photonics Reviews*, vol. 7, no. 1, pp. 45–59, 2013.

[61] I. Vera-Marun, P. Zomer, A. Veligura, M. Guimarães, L. Visser, N. Tombros, H. van Elferen, U. Zeitler, and B. van Wees, "Quantum hall transport as a probe of capacitance profile at graphene edges," *Applied Physics Letters*, vol. 102, no. 1, p. 013106, 2013.

[62] A. Beukman, "Topology in two-dimensional systems," 2016.

[63] K. Suzuki, Y. Harada, F. Maeda, K. Onomitsu, T. Yamaguchi, and K. Muraki, "Gate operation of inas/algasb heterostructures with an atomic-layer-deposited insulating layer," *Applied Physics Express*, vol. 4, no. 12, p. 125702, 2011.

[64] K. Shibata, M. Karalic, C. Mittag, T. Tschirky, C. Reichl, H. Ito, K. Hashimoto, T. Tomimatsu, Y. Hirayama, W. Wegscheider, T. Ihn, and K. Ensslin, "Electric-field-induced two-dimensional hole gas in undoped gasb quantum wells," *Applied Physics Letters*, vol. 114, no. 23, p. 232102, 2019.

[65] B. I. Shklovskii and A. L. Efros, *Electronic Properties of Doped Semiconductors*. Springer-Verlag, Berlin, 1984.

[66] M. Bockrath, D. H. Cobden, J. Lu, A. G. Rinzler, R. E. Smalley, L. Balents, and P. L. McEuen, "Luttinger-liquid behaviour in carbon nanotubes," *Nature*, vol. 397, pp. 598 EP –, Feb 1999.

[67] A. Kanda, K. Tsukagoshi, Y. Aoyagi, and Y. Ootuka, "Gate-voltage dependence of zero-bias anomalies in multiwall carbon nanotubes," *Phys. Rev. Lett.*, vol. 92, p. 036801, Jan 2004.

[68] S. V. Zaitsev-Zotov, Y. A. Kumzerov, Y. A. Firsov, and P. Monceau, "Luttinger-liquid-like transport in long InSb nanowires," *Journal of Physics: Condensed Matter*, vol. 12, pp. L303–L309, may 2000.

[69] E. Slot, M. A. Holst, H. S. J. van der Zant, and S. V. Zaitsev-Zotov, "One-dimensional conduction in charge-density-wave nanowires," *Phys. Rev. Lett.*, vol. 93, p. 176602, Oct 2004.

[70] A. N. Aleshin, H. J. Lee, Y. W. Park, and K. Akagi, "One-dimensional transport in polymer nanofibers," *Phys. Rev. Lett.*, vol. 93, p. 196601, Nov 2004.

[71] L. Venkataraman, Y. S. Hong, and P. Kim, "Electron transport in a multichannel one-dimensional conductor: Molybdenum selenide nanowires," *Phys. Rev. Lett.*, vol. 96, p. 076601, Feb 2006.

[72] A. S. Rodin and M. M. Fogler, "Apparent power-law behavior of conductance in disordered quasi-one-dimensional systems," *Phys. Rev. Lett.*, vol. 105, p. 106801, Sep 2010.

[73] R. Winkler, "Spin-orbit coupling effects in two-dimensional electron and hole systems," *Springer Tracts in Modern Physics*, vol. 191, pp. 1–8, 2003.

[74] J. Fabian, A. Matos-Abiague, C. Ertler, P. Stano, and I. Žutić, "Semiconductor spintronics," *Acta Physica Slovaca. Reviews and Tutorials*, vol. 57, no. 4-5, pp. 565–907, 2007.

[75] G. Dresselhaus, "Spin-orbit coupling effects in zinc blende structures," *Physical Review*, vol. 100, no. 2, p. 580, 1955.

[76] F. J. Ohkawa and Y. Uemura, "Quantized surface states of a narrow-gap semiconductor," *Journal of the Physical Society of Japan*, vol. 37, no. 5, pp. 1325–1333, 1974.

[77] Y. A. Bychkov and E. I. Rashba, "Oscillatory effects and the magnetic susceptibility of carriers in inversion layers," *Journal of physics C: Solid state physics*, vol. 17, no. 33, p. 6039, 1984.

[78] C. Schierholz, *Rashba Spin-Orbit Interaction in Low and High Magnetic Fields*. Cuvillier Verlag, 2005.

[79] A. Ström, H. Johannesson, and G. I. Japaridze, "Edge dynamics in a quantum spin hall state: Effects from rashba spin-orbit interaction," *Phys. Rev. Lett.*, vol. 104, p. 256804, Jun 2010.

[80] F. m. c. Crépin, J. C. Budich, F. Dolcini, P. Recher, and B. Trauzettel, "Renormalization group approach for the scattering off a single rashba impurity in a helical liquid," *Phys. Rev. B*, vol. 86, p. 121106, Sep 2012.

[81] F. Geissler, F. m. c. Crépin, and B. Trauzettel, "Random rashba spin-orbit coupling at the quantum spin hall edge," *Phys. Rev. B*, vol. 89, p. 235136, Jun 2014.

[82] A. Manchon, H. C. Koo, J. Nitta, S. M. Frolov, and R. A. Duine, "New perspectives for rashba spin-orbit coupling.," *Nature materials*, vol. 14 9, pp. 871–82, 2015.

[83] A. J. A. Beukman, F. K. de Vries, J. van Veen, R. Skolasinski, M. Wimmer, F. Qu, D. T. de Vries, B.-M. Nguyen, W. Yi, A. A. Kiselev, M. Sokolich, M. J. Manfra, F. Nichele, C. M. Marcus, and L. P. Kouwenhoven, "Spin-orbit interaction in a dual gated inas/gasb quantum well," *Phys. Rev. B*, vol. 96, p. 241401, Dec 2017.

[84] F. Herzog, H. Hardtdegen, T. Schäpers, D. Grundler, and M. Wilde, "Experimental determination of rashba and dresselhaus parameters and g*-factor anisotropy via

shubnikov-de haas oscillations," *New Journal of Physics*, vol. 19, no. 10, p. 103012, 2017.

[85] F. Nichele, M. Kjaergaard, H. J. Suominen, R. Skolasinski, M. Wimmer, B.-M. Nguyen, A. A. Kiselev, W. Yi, M. Sokolich, M. J. Manfra, F. Qu, A. J. A. Beukman, L. P. Kouwenhoven, and C. M. Marcus, "Giant spin-orbit splitting in inverted $\mathrm{InAs/GaSb}$ double quantum wells," *Phys. Rev. Lett.*, vol. 118, p. 016801, Jan 2017.

[86] R. Fiederling, M. Keim, G. Reuscher, W. Ossau, G. Schmidt, A. Waag, and L. W. Molenkamp, "Injection and detection of a spin-polarized current in a light-emitting diode," *Nature*, vol. 402, no. 6763, pp. 787–790, 1999.

[87] C. Brüne, A. Roth, H. Buhmann, E. M. Hankiewicz, L. W. Molenkamp, J. Maciejko, X.-L. Qi, and S.-C. Zhang, "Spin polarization of the quantum spin hall edge states," *Nature Physics*, vol. 8, pp. 485 EP –, May 2012. Article.

[88] J. Luo, H. Munekata, F. F. Fang, and P. J. Stiles, "Effects of inversion asymmetry on electron energy band structures in gasb/inas/gasb quantum wells," *Phys. Rev. B*, vol. 41, pp. 7685–7693, Apr 1990.

[89] B. Jusserand, D. Richards, G. Allan, C. Priester, and B. Etienne, "Spin orientation at semiconductor heterointerfaces," *Physical Review B*, vol. 51, no. 7, p. 4707, 1995.

[90] J. Nitta, T. Akazaki, H. Takayanagi, and T. Enoki, "Gate control of spin-orbit interaction in an inverted i n 0.53 g a 0.47 as/i n 0.52 a l 0.48 as heterostructure," *Physical Review Letters*, vol. 78, no. 7, p. 1335, 1997.

[91] G. Engels, J. Lange, T. Schäpers, and H. Lüth, "Experimental and theoretical approach to spin splitting in modulation-doped $\mathrm{in_x ga_{1-x} as/inp}$ quantum wells for b→0," *Phys. Rev. B*, vol. 55, pp. R1958–R1961, Jan 1997.

[92] J. Heida, B. Van Wees, J. Kuipers, T. Klapwijk, and G. Borghs, "Spin-orbit interaction in a two-dimensional electron gas in a inas/alsb quantum well with gate-controlled electron density," *Physical Review B*, vol. 57, no. 19, p. 11911, 1998.

[93] C.-M. Hu, J. Nitta, T. Akazaki, H. Takayanagi, J. Osaka, P. Pfeffer, and W. Zawadzki, "Zero-field spin splitting in an inverted in 0.53 ga 0.47 a s/i n 0.52 al 0.48 as heterostructure: Band nonparabolicity influence and the subband dependence," *Physical Review B*, vol. 60, no. 11, p. 7736, 1999.

[94] S. Brosig, K. Ensslin, R. Warburton, C. Nguyen, B. Brar, M. Thomas, and H. Kroemer, "Zero-field spin splitting in inas-alsb quantum wells revisited," *Physical Review B*, vol. 60, no. 20, p. R13989, 1999.

[95] S. Papadakis, E. De Poortere, H. Manoharan, M. Shayegan, and R. Winkler, "The effect of spin splitting on the metallic behavior of a two-dimensional system," *Science*, vol. 283, no. 5410, pp. 2056–2058, 1999.

[96] D. Grundler, "Large rashba splitting in inas quantum wells due to electron wave function penetration into the barrier layers," *Physical review letters*, vol. 84, no. 26, p. 6074, 2000.

[97] Z. J. Qiu, Y. S. Gui, T. Lin, N. Dai, J. H. Chu, N. Tang, J. Lu, and B. Shen, "Weak localization and magnetointersubband scattering effects in an $al_x ga_{1-x} N/GaN$ two-dimensional electron gas," *Phys. Rev. B*, vol. 69, p. 125335, Mar 2004.

[98] F. V. Tikhonenko, D. W. Horsell, R. V. Gorbachev, and A. K. Savchenko, "Weak localization in graphene flakes," *Phys. Rev. Lett.*, vol. 100, p. 056802, Feb 2008.

[99] M. Studer, G. Salis, K. Ensslin, D. C. Driscoll, and A. C. Gossard, "Gate-controlled spin-orbit interaction in a parabolic $GaAs/AlGaAs$ quantum well," *Phys. Rev. Lett.*, vol. 103, p. 027201, Jul 2009.

[100] B. A. Assaf, T. Cardinal, P. Wei, F. Katmis, J. S. Moodera, and D. Heiman, "Linear magnetoresistance in topological insulator thin films: Quantum phase coherence effects at high temperatures," *Applied Physics Letters*, vol. 102, no. 1, p. 012102, 2013.

[101] B. Shojaei, P. O'Malley, J. Shabani, P. Roushan, B. Schultz, R. Lutchyn, C. Nayak, J. Martinis, and C. Palmstrøm, "Demonstration of gate control of spin splitting in a high-mobility inas/alsb two-dimensional electron gas," *Physical Review B*, vol. 93, no. 7, p. 075302, 2016.

[102] F. Herling, C. Morrison, C. S. Knox, S. Zhang, O. Newell, M. Myronov, E. H. Linfield, and C. H. Marrows, "Spin-orbit interaction in inas/gasb heterostructures quantified by weak antilocalization," *Phys. Rev. B*, vol. 95, p. 155307, Apr 2017.

[103] M. Meng, S. Huang, C. Tan, J. Wu, Y. Jing, H. Peng, and H. Q. Xu, "Strong spin–orbit interaction and magnetotransport in semiconductor bi2o2se nanoplates," *Nanoscale*, vol. 10, pp. 2704–2710, 2018.

[104] L. Wang, M. Yin, A. Khan, S. Muhtadi, F. Asif, E. S. Choi, and T. Datta, "Scatterings and quantum effects in $(\mathrm{Al}, \mathrm{In})\mathrm{N}/\mathrm{GaN}$ heterostructures for high-power and high-frequency electronics," *Phys. Rev. Applied*, vol. 9, p. 024006, Feb 2018.

[105] M. Brahlek, N. Koirala, N. Bansal, and S. Oh, "Transport properties of topological insulators: Band bending, bulk metal-to-insulator transition, and weak anti-localization," *Solid State Communications*, vol. 215, pp. 54–62, 2015.

[106] S. Hikami, A. I. Larkin, and Y. Nagaoka, "Spin-Orbit Interaction and Magnetoresistance in the Two Dimensional Random System," *Progress of Theoretical Physics*, vol. 63, pp. 707–710, 02 1980.

[107] S. Iordanskii, Y. B. Lyanda-Geller, and G. Pikus, "Weak localization in quantum wells with spin-orbit interaction," *ZhETF Pisma Redaktsiiu*, vol. 60, p. 199, 1994.

[108] Y. Niimi, Y. Baines, T. Capron, D. Mailly, F.-Y. Lo, A. D. Wieck, T. Meunier, L. Saminadayar, and C. Bäuerle, "Quantum coherence at low temperatures in mesoscopic systems: Effect of disorder," *Phys. Rev. B*, vol. 81, p. 245306, Jun 2010.

[109] B. L. Altshuler, A. G. Aronov, and D. E. Khmelnitsky, "Effects of electron-electron collisions with small energy transfers on quantum localisation," *Journal of Physics C: Solid State Physics*, vol. 15, pp. 7367–7386, dec 1982.

[110] R. Taboryski and P. E. Lindelof, "Weak localisation and electron-electron interactions in modulation-doped GaAs/AlGaAs heterostructures," *Semiconductor Science and Technology*, vol. 5, pp. 933–946, sep 1990.

Appendix A: A SHORT DISCUSSION ON OUR HETEROSTRUC-TURES

A.1. Comparison of 3 different InAs/GaSb double quantum well heterostructures

We designed three wafer structures and have them grown by standard molecular beam epitaxy (MBE) method. The heterstructure of wafers A, B, and C are shown in figures 3.3, 4.3, and A.2, respectively. Wafers A and B were characterized in chapters 3 and 4, respectively. Table A.1 compares these heterostructures briefly.

Table A.1: Comparison of heterostructures

	Wafer A	**Wafer B**	**Wafer C**
Substrate	GaAs	GaAs	GaSb
Upper barrier	$Al_{0.8}Ga_{0.2}Sb$ (50 nm)	$Al_{0.8}Ga_{0.2}Sb$ (50 nm)	$Al_{0.8}Ga_{0.2}Sb$ (50 nm)
Lower barrier	$Al_{0.8}Ga_{0.2}Sb$ (50 nm)	$Al_{0.8}Ga_{0.2}Sb$ (50 nm)	$Al_{0.8}Ga_{0.2}Sb$ (50 nm)
InAs/GaSb thickness	12 nm / 9 nm	12.5 nm / 10 nm	12 nm / 9 nm
Si concentration	1×10^{11} cm^{-2}	1×10^{11} cm^{-2}	1×10^{11} cm^{-2}
Si position relative to InAs/GaSb interface	0.6 nm inside InAs	0.3 nm inside InAs	0.3 nm inside GaSb

Substrates: Wafers A and B were grown on GaAs substrates for which one needs to grow a thicker buffer layer below AlGaSb/InAs/GaSb/AlGaSb double quantum well layers. The buffer helps to relax the crystal defects and dislocations due to slightly mismatched epilayers with the GaAs substrate. However, the GaSb crystal structure, on which the wafer C was grown, is more compatible with the QWs lattices. Suppression of crystal defects are critically important to reduce the charge trap states at the interfaces and also to improve the bottom gate performance for minimum gate current leakage.

QWs thickness: The relative thickness of the InAs/GaSb QWs in these three heterstructures are similar. Wafers A and C have exactly the same bilayer QWs (12 nm InAs/ 9 nm GaSb), while for wafer B, a 12.5 nm InAs/ 10 nm GaSb double QW was grown. In theory, this slight difference in relative thicknesses of InAs/GaSb is not expected to cause
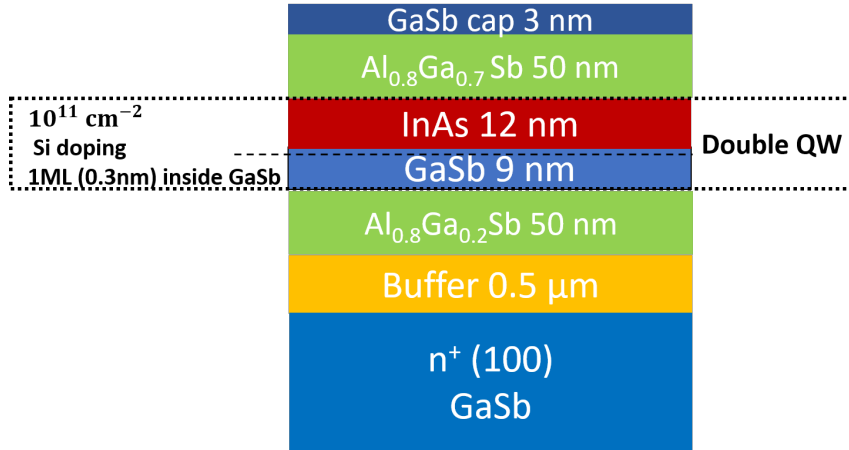
Figure A.2: Wafer C grown on GaSb substrate with a thinner buffer layer since the substrate is better matched with epilayers compared to GaAs substrates used for A and B.

a significant difference in band alignment. Referencing to [12], the band alignment is particularly more sensitive to InAs layer thickness. Therefore, the very different transport behavior we observed for wafer B can not be related to its different bilayer thickness. We believe that the position of silicon delta-doping in our heterostructures plays a critical role in their transport properties.

Si-disorder position: The Si delta-like atoms had been deposited during the epitaxial growth of the hetero-layers at a given z-position in the growth direction close to the InAs/GaSb interface. Silicon impurities with an average density of 10^{11} cm^{-2} are deposited within a single layer inside InAs at respectively two and one atomic layer distance from InAs/GaSb interface for wafers A and B. In wafer C, they are located in GaSb one single atomic layer off from the interface of Qws. Silicon atom behaves as a donor in InAs and an acceptor in GaSb. As a donor, it attracts the electron band without interacting the hole band. Similarly, as an acceptor, it pushes the hole band leaving the electron band noninteracted. Some numerical analysis have shown that impurities of any type, donor or acceptor, would results in formation of localized states inside the hybridization gap of band-inverted InAs/GaSb bilayers. However, an experimental proof would require a variety of wafers with different types of disorder with various strengths. Inspiring from Ref. [22], we disordered our heterostructures by Si atoms at different positions and layers of double QWs. Later in this chapter we will argue the possible effect of silicon disorder and its position in transport behavior, which indeed led to quite different characteristics in our wafers.
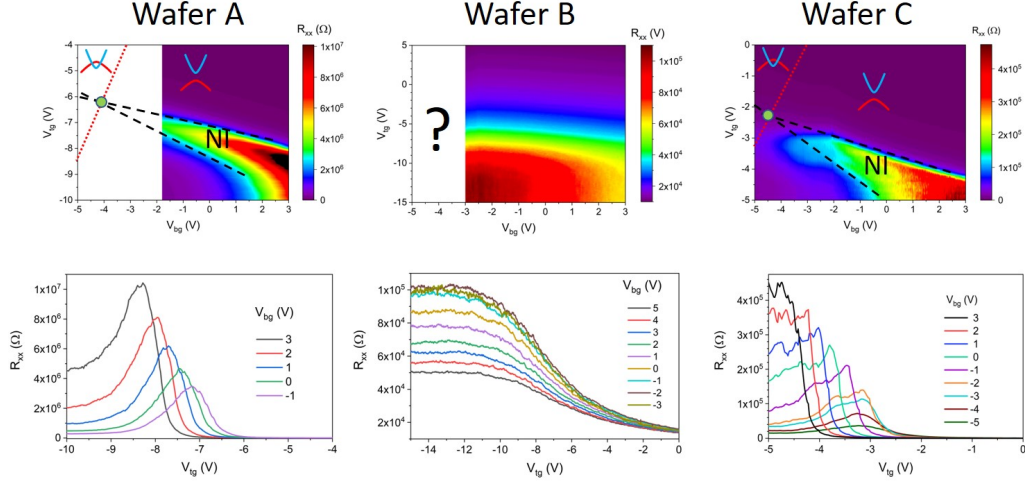
Figure A.3: Upper panels: Comparison of Phase diagram for wafers A, B, and C. For wafer A, only a trivial band regime is accessible within the range of applicable bottom gate voltages. wafer C shows similar phases as for wafer A, but with an expandable bottom gate voltages towards inverted band phase. Wafer B behaves completely different showing plateau-like resistances which increase at lowered V_{bg} unlike the other two wafers. Lower panels: The cross section of corresponding phase diagrams at specific bottom gate voltages .

A.2. Phase diagram characterization

The phase diagram of 3 wafers in gate voltage space is compared in Fig. A.3. Wafers A and C exhibit similar resistance modulation by top and bottom gates. Whereas, wafer B behaves totally different like a semi-metal with unexplained resistance plateaus at different values for different V_{bg}.

A.2.1. Bottom gate

Wafers A and B which are grown on GaAs substrates have the issue of bottom gate performance. That is the bottom gate starts to leak below -2 to -3 volts. Wafer C benefiting from GaSb substrate has the best gate operation where the bottom gate voltages down to -5 V is applicable without significant current leakage. GaSb substrates are preferable for epitaxial growth of InAs/GaSb-based heterostructures because its crystal mismatch is reduced compared to GaAs substrates. In addition, this compatibility allows for thinner buffer layer which in turn enhance the effective electric field within the same range of bottom gate voltage. The wider range of bottom and top gate voltages allow to probe the full phase diagram of the InAs/GaSb structures predicted by theory.

A.2.2. Band alignment by gates

Top and bottom gates together can modulate the alignment between the InAs electron band and GaSb hole band. At the same time the potential in the QWs i.e. the Fermi level is set by dual gate electrodes. Therefore, the gates should be able to tune the energy gap in non-inverted regime and band overlap in the inverted regime.

Wafer A, discussed in chapter 3, displays a well defined trivial regime with a gap controlled by gate voltages. However, the bottom gate voltage is limited due to current leakage. Therefore, the voltages $V_{bg} \leq -2$ V could not be explored. The corresponding accessible phase diagram is shown in A.3. The dashed line indicates the trivial gap region. They would be expected to cross at $V_{bg} \sim -4$ V where the trivial gap closes and bands start to overlap (inverted regime). Similar phase diagram was obtained for wafer C with identical Qw thicknesses as for A but with GaSb substrate and Si doping inside GaSb QW. Again dashed lines ar guidelines showing the edges of the bands. The longitudinal resistances in wafer C is one order of magnitude smaller than wafer A in the trivial insulating regime, which indicates that the trivial edge states are more effectively localized in wafer A. We emphasize that wafer C is not fully characterized yet. The inverted regime and the peculiar flat part in the phase diagram needs further studies. The resistance behavior with top and bottom gate voltages in wafer B is completely different than the A and C. Longitudinal resistance develops to plateau-like regions in the top gate sweeps for all bottom gate voltages. No signature of a trivial gap behavior is observed. We could not explain this behavior and can not confirm if it is in inverted or non-inverted regime.

A.3. Silicon disorder

Silicon disorder was first introduced by Ref. [22] to localize the excess bulk carriers in the hybridization gap which can otherwise mask the topological edge conduction. A silicon atom at the InAs/GaSb interface, serving as a donor in InAs and an acceptor in GaSb, was expected to interact with both electrons and holes thus to localize the bulk carriers in the hybridization gap. However, the effect of disorder on the trivial regime was not investigated and the hole phase diagram in the presence and absence of such disorder was not compared. The residual bulk conductivity in the inverted gap regime is a common issue in these QSH candidate. It is believed to stem from the potential fluctuations which excite the bulk carriers in the relatively small inverted gap of a few meV (30 - 40 K). Later a couple of theoretical studies examined the Si disorder effects on the inverted regime of InAs/GaSb QWs. They showed that in-gap states are formed by silicon disorder, which localizes the bulk carriers. However, a comprehensive study

on the effect of disorder on transport behavior in all regimes including trivial regime is still missing. Moreover, the influence of disorder's strength, type, and position on the band alignment would help to better understand the electronic properties of InAs/GaSb bilayer systems. For example, it is known that edge states also exist in the trivial gap and may coexist with expected helical edge states in the inverted regime as well. Unlike QSH edge channels which are topologically protected against disorder, the trivial edge modes can be easily localized by an arbitrary disorder strength. Elimination of trivial edge conduction is an important step towards a robust QSHE in InAs/GaSb double QW systems. In this thesis, we accomplished the localization of trivial edge states in normal gap region. Having the Si disorder deeper inside InAs layer seems to be most effective in trivial edge states' localization.

Although wafers A and B presents similar behavior in trivial regime, the position of silicon disorder relative to the interface of InAs/GaSb layers sounds to be important. In both wafers, the trivial gap is tuned by dual gate voltages, however, the trivial edge states are localized to different extent. Localization of trivial edge states in wafer A was investigated in chapter 3. Wafer C shows similar behavior but with resistances of one order of magnitude smaller. Assuming that the trivial edge states are electron-type thus originated from InAs band, the impurity inside InAs layer would be more effective to localize trivial edge carriers compared to the one located inside GaSb QW layer.

On the other hand, wafer B, with Si impurities only one monolayer closer to the interface compared to wafer A, exhibited a disordered semi-metallic behavior. No activated gap behavior was observed in this structure. Indeed, a 2D weak localization regime in this wafer was studied in chapter 4, where we observed WAL/WL features in magnetotranport measurements. The mobility of this wafer ($\mu \sim 1000 \text{ cm}^2/\text{Vs}$) was found at least an order of magnitude smaller than wafer A. In wafer A, the silicon atoms are 2 atomic layers far from the interface thus predominantly affect the InAs than GaSb charge carriers. Whereas in wafer B, they are closer to the interface and perhaps influence both QWs. We believe that the potential fluctuations induced by Si impurities in this wafer is so strong that may hinder the bulk gap either trivial or non-trivial leading to a semi-metallic behavior. A full understanding of the transport characteristics of wafer B needs further studies.

Appendix B: SAMPLE FABRICATION

The InAs/GaSb composite quantum wells are meant to be tunable between trivial and topological phases by dual gate electrodes. Therefore the fabrication processes should be optimized for best top and bottom gate performances. A standard fabrication recipe includes hot-plate baking for resist coating, lithography to define the patterns, etching to isolate the device's mesa, passivation of the etched edges, and metalization of the ohmioc contacts and the top gate electrodes.

The common issue for back gate is the current leakage through the bottom surface of the heterostructures, which can be improved by using a GaSb instead of a GaAs substrate. However, for a given wafer structure, the back gate performance is strongly dependent on the fabrication processes a sample goes through. We performed a comprehensive test experiments to rule out the possible fabrication-induced reasons for bottom gate leakage. We realized that the dry etching and high temperature ($>200\,°C$) annealing have detrimental effects on the back gate performance. The ion bombardment during the dry etching process may damage the heterostructure which in turn leads to a leakage through back gate. Moreover, the annealing of the ohmic contacts enhances the metal diffusion which may short the contact to the bottom gate. Therefore, in this study, we used wet etching methods and made annealing-free ohmic contacts to avoid any possible fabrication related damage on the heterostructure thus to minimize the back gate current leakage.

The InAs/GaSb-based heterostructures are usually capped with a thin GaSb layer for protection against oxidization. It is known that at the interface of GaSb and the dielectric or oxide layers, there exist charge trap states which screen the top gate electric field and change the effective top gate voltage on the QW structures. It is manifested by a hysteresis in the forward and backward top gate voltage sweep. The amount of hysteresis depends on the surface treatment, passivation method, layers interface effects, the QW barriers, and the passivation dielectric material and thickness. We have always the hysteresis in top gate sweep for all heterostructures and with different passivation layers. However, a thick dielectric layer needs a higher gate voltage bias which enhances the charge trapping at the interface between GaSb and the dielectric. Therefore, it is important to have thinner dielectric layer to reduce the charge trapping thus the hysteresis.
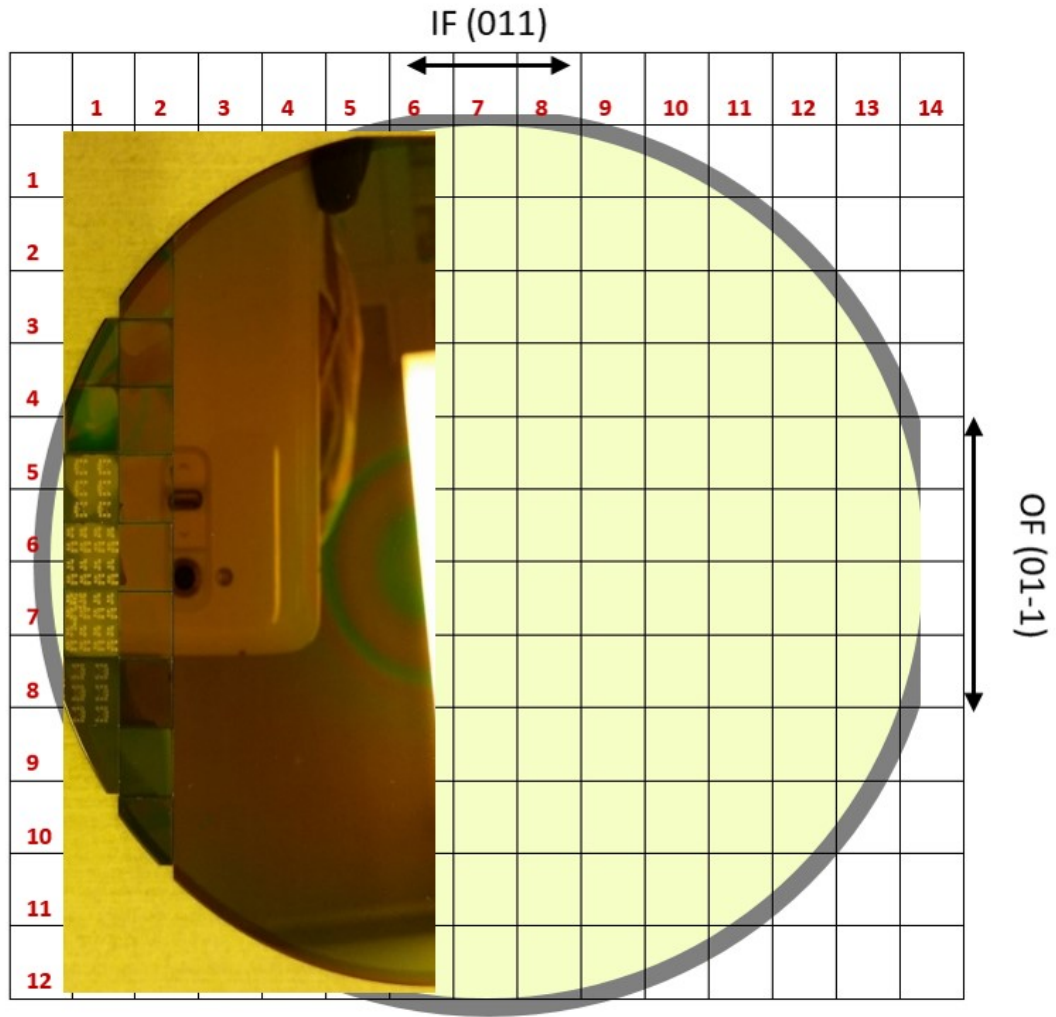
Figure B.1: The dicing map for a 4-inch wafer. Individual pieces are labeled as matrix elements with their corresponding row and column numbers.

Starting from standard fabrication recipes, we developed a recipe with a focus on minimization of the bottom gate leakage. However, one should bear in mind that a recipe would not necessarily give the same results under nominally the same circumstances. From place to place or sample to sample, you may get remarkably different devices. The devices in this study were fabricated with the following recipe.

B.1. OHMIC CONTACTS

- Dice the wafer into 6×7 mm^2 pieces (see Fig. B.1 for wafer map). Each piece can host 4 individual samples to be mounted on separate chip carriers.

- Clean the wafer piece in acetone and isopropanol alcohol (IPA) and dry with nitrogen gas.

- Spin coating of MMA EL11 e-beam resist at 5000 rpm for 60 seconds.

- Hot plate baking at $170\,^\circ$C

- Spin coating of PMMA 950C2 e-beam resist at 5000 rpm for 60 seconds.

- Hot plate baking at $170\,^\circ$C

- Electron beam lithography for patterning the ohmic contacts.

- Developing the exposed e-beam resist with MIBK:IPA (1:3) for 60 seconds followed by 10 second extra develop in MIBK:IPA (1:1) to ensure the complete removal of the resist. Rinse with IPA to remove residual developer.

- Deposition of ohmic metals: Ge/Au/Ni/Au (18 nm/50 nm/18 nm/100 nm).

- Lift-off in hot acetone for about half an hour.

B.2. E-BEAM LITHOGRAPHY TO DEFINE THE DEVICE STRUCTURE

- Clean the wafer piece in acetone and IPA, and dry with nitrogen gas.

- Spin coating of PMMA 950A5 e-beam resist at 5000 rpm for 60 seconds.

- Hot plate baking at $170\,^\circ$C

- Electron beam lithography for patterning the device's mesa.

- Developing the exposed e-beam resist with MIBK:IPA (1:3) for 60 seconds. Rinse with IPA to remove residual developer.

B.3. WET ETCHING TO ISOLATE THE MESA

- Preparation of the etchant solution: Blend and steer H_3PO_4:H_2O_2 : $C_6H_8O_7$:H_2O with a volume ratio of 3:5:55:220. We used ortho-phosphoric acid 85%, hydrogen peroxide 35%, and citric acid solution of 33%. The citric acid solution is made by dissolving x grams dehydrated citric acid powder into $2x$ ml DI water. The average etching rate of the mixture is 50 - 60 nm/min.

- Etch the heterostructure for 3 minutes to isolate the device's mesa. Rinse with DI water to stop etching.

- Remove the PMMA with acetone, rinse with IPA, and dry.

B.4.   PASSIVATION OF ETCHED WALLS

- Immediately after etching and resist removal, load the sample into the PECVD chamber. The side walls of etched mesa can be oxidized quickly when exposed to the air.

- Grow SiN_x of about 100 nm thickness for edge passivation and also as dielectric for top gating. The growth rate of our PECVD recipe was 20-25 nm/min at $180\,°C$.

B.5.   TOP GATE

- Clean the wafer piece in acetone and IPA, and dry with nitrogen gas.

- Spin coating of MMA EL11 e-beam resist at 5000 rpm for 60 seconds.

- Hot plate baking at $170\,°C$

- Spin coating of PMMA 950C2 e-beam resist at 5000 rpm for 60 seconds.

- Hot plate baking at $170\,°C$

- Electron beam lithography for patterning the top gate.

- Develop the exposed e-beam resist with MIBK:IPA (1:3) for 60 seconds followed by 10 second extra develop in MIBK:IPA (1:1) to ensure the complete removal of the resist. Rinse with IPA to remove residual developer.

- Deposition of Ti/Au (5 nm/100 nm).

- Lift-off in hot acetone for about half an hour.

B.6.   ACCESS TO THE OHMIC CONTACTS

- Clean the wafer piece in acetone and IPA, and dry with nitrogen gas.

- Spin coating of PMMA 950A5 e-beam resist at 5000 rpm for 60 seconds.

- Hot plate baking at $170\,°C$

- Electron beam lithography for patterning the ohmics access.

- Develop the exposed e-beam resist with MIBK:IPA (1:3) for 60 seconds. Rinse with IPA to remove residual developer.

- Etch the SiN_x insulator layer with BOE for 20 seconds to open the access to the ohmic wiring pads. Rinse with DI water and dry.

B.7.   WIRE BONDING

- Cut the processed wafer piece into 4 chips.

- Clean the samples in acetone and IPA, and dry with nitrogen gas.

- Mount each individual sample on a chip carrier using the twin silver epoxy EPO-TEK H20E cured at $150\,°C$ for 5 minutes.

- Wire bond the ohmic and top gate contacts manually with the use of H20E silver epoxy cured at $150\,°C$ for 5 minutes. It is important to bond the wires manually to eliminate any risk of electronic short between back gate and the QWs due to possible damage a wire bonder machine can make.